Aalto University
School of Science
Degree Programme in Engineering Physics and Mathematics

Maarit Aro

Functional Magnetic Resonance Imaging During Natural Viewing

Master's Thesis
Espoo, April 23, 2015

Supervisor: Academy Professor Risto Ilmoniemi, Aalto University
Advisors: Professor Riitta Hari, Aalto University
Sanna Malinen D.Sc. (Tech)

Aalto University
School of Science
Degree Programme in Engineering Physics and Mathematics

ABSTRACT OF
MASTER'S THESIS

Author: Maarit Aro

Title:
Functional Magnetic Resonance Imaging During Natural Viewing

Date: April 23, 2015 **Pages:** vi + 59

Major: Biomedical Engineering **Code:** F3001

Supervisor: Academy Professor Risto Ilmoniemi
Advisors: Professor Riitta Hari
Sanna Malinen D.Sc. (Tech)

Functional magnetic resonance imaging (fMRI) is based on changes in the brain's haemodynamics that are coupled to neural activations. FMRI enables the study of brain functions during various stimuli and tasks. Recent developments in brain imaging technology allow more complex and natural experimental setups, and subsequently also new analysis techniques are required to extract the information from the measured signals. The aim of this thesis was to study information processing in the human brain during natural viewing conditions. The imaging data were analyzed with two different methods.

We collected fMRI data from eight subjects, who were viewing a still or a moving bird against a naturalistic landscape or a gray background. We studied activations of different visual areas during the different stimulus conditions. The results of analysis based on general linear model (GLM), which is currently the most common approach to analyze fMRI data, were compared with results of independent component analysis (ICA), a data-driven analysis tool. ICA separates spatially independent signal sources and their time courses from the measured fMRI data.

Both methods revealed activations in the posterior visual areas. GLM-based analysis showed different activation patterns for the different stimuli so that the moving bird activated visual motion areas and the naturalistic environment early visual areas and visual object areas. ICA separated several vision-related ICs, covering, e.g., the early visual cortices for central and peripheral visual fields, and the visual motion areas. These components had distinct time courses with different reactions to the different stimulus blocks. In general, the results obtained by the two analysis methods were consistent, but both ICA and GLM also showed activations that the other method missed. In the future, new approaches would be needed for fMRI data analysis to gain knowledge of brain processing of complex and varying stimuli in naturalistic settings.

Keywords: functional magnetic resonance imaging, general linear model, GLM, ICA, independent component analysis, naturalistic stimuli, visual cortex, visual motion

Language: English

Aalto-yliopisto
Perustieteiden korkeakoulu
Teknillisen fysiikan ja matematiikan koulutusohjelma

DIPLOMITYÖN TIIVISTELMÄ

Tekijä:	Maarit Aro		
Työn nimi:	Toiminnallinen magneettiresonanssikuvaus luonnollisessa katselutilanteessa		
Päiväys:	23. huhtikuuta 2015	**Sivumäärä:**	vi + 59
Pääaine:	Lääketieteellinen tekniikka	**Koodi:**	F3001
Valvoja:	Akatemiaprofessori Risto Ilmoniemi		
Ohjaajat:	Professori Riitta Hari Tekniikan tohtori Sanna Malinen		

Toiminnallinen magneettikuvaus (fMRI) perustuu aivojen verenkierron muutoksiin, jotka ovat yhteydessä aivoalueiden neuraaliseen aktivaatioon. FMRI mahdollistaa aivojen toiminnan seuraamisen erilaisten ärsykkeiden ja tehtävien aikana. Aivokuvantamismenetelmien kehitys viime vuosina on mahdollistanut yhä monimutkaisemmat ja luonnollisemmat mittausasetelmat, ja myös data-analyysiin vaaditaan uudenlaisia lähestymistapoja. Tässä työssä perehdyttiin näköinformaation käsittelyyn aivoissa luonnonmukaisessa katselutilanteessa kahden eri analyysimenetelmän avulla.

Työssä mitattiin kahdeksan koehenkilön aivotoimintaa fMRI:n avulla heidän seuratessaan kuvaruudulla lintua, joka joko pysyi paikoillaan tai liikkui joko luonnollisessa ulkoympäristössä tai harmaalla taustalla. Työssä pyrittiin tutkimaan, kuinka informaation prosessointi näköaivokuoren eri alueilla eroaa toisistaan näissä tilanteissa. Datan käsittelyssä vertailtiin yleiseen lineaarinen malliin (GLM) perustuvaa menetelmää, joka on tällä hetkellä yleisin fMRI-datan analyysimenetelmä, sekä spatiaalista riippumattomien komponenttien menetelmää (ICA), joka pyrkii erottamaan signaalijoukosta niiden taustalla olevat riippumattomat komponentit sekä niihin liittyvät aikasarjat.

Molemmat menetelmät erottelivat selkeitä aktivaatiota näköaivokuorilla. GLM-analyysin mukaan liikkuva lintu aiheutti merkittävimmät aktivaatiot visuaalisilla liikealueilla ja luonnollinen tausta aktivoi primaarisia näköaivoalueita sekä näköaivokuoren objektialueita. ICA erotteli datasta erillisiä komponentteja, jotka vastasivat esimerkiksi primaarisen näköaivokuoren keskeis- ja perifeerisen näön alueita sekä visuaalisia liikealueita. Myös komponenttien aikakäyttäytymiset erosivat toisistaan. Monet GLM- ja ICA-analyysin aktivaatiot vastasivat toisiaan, mutta menetelmät paljastivat myös toisistaan eroavia tuloksia. Tulevaisuudessa tunnettujen ja uusien menetelmien kehitys jatkuu, jotta entistä monipuolisemmissa koetilanteissa mitattujen aivosignaalien tulkinta olisi mahdollista.

Asiasanat:	GLM, ICA, luonnolliset ärsykkeet, näköaivokuori, riippumattomien komponenttien menetelmä, toiminnallinen magneettikuvaus, yleinen lineaarinen malli, visuaalinen liike
Kieli:	Englanti

Acknowledgements

This study was carried out at the Brain Research Unit of the Aalto University School of Science. The work was financially supported by the Academy of Finland (National Centers of Excellence Programme 2006–2011) and Sigrid Jusélius Foundation.

I would like to thank the instructors of this thesis, Professor Riitta Hari and D.Sc. (Tech) Sanna Malinen for excellent guidance during the project. I thank Riitta for providing me the possibility of working in this interesting research field and for offering her expert knowledge, advice and support. Sanna, being my closest co-worker in this project, contributed significantly to every step of it. I really appreciated all her help and dedication to this work, as well as her good company. I also thank Prof. Risto Ilmoniemi for his comments and improvements on language.

I also would like to thank Katja Korhonen for stimulus videos, M.Sc.(Tech) Veli-Matti Saarinen for the analysis of eye-tracking data, and radiographer Marita Kattelus for assistance and expert help in fMRI experiments. The positive and stimulating atmosphere of the lab made working here a highly enjoyable experience and owes thanks to all my co-workers.

Espoo, April 23, 2015

Maarit Aro

Contents

Chapter 1

Introduction

Functional magnetic resonance imaging (fMRI) is a brain-imaging method based on changes in blood oxygenation level in the blood flow of the brain; these changes are connected to changes in neuronal activation. The MRI signal arises when protons, primarily found in tissue water and in lipids, interact with a magnetic field [1]. Measuring the changes in fMRI signal enables to study activations and deactivations in different brain regions. This thesis focuses on brain processing of visual information during viewing of naturalistic scene as reflected by fMRI. Cortical processing of visual information starts in the early visual cortices, especially the primary visual cortex (V1), and involves after that several other brain areas.

In this work I aimed to study information processing in the human brain while subjects were viewing both continuously changing stimuli and still images in a naturalistic environment. Independent component analysis (ICA) was applied to separate spatially independent signal sources from the measured fMRI data. The results of ICA were compared with results obtained from an approach based on general linear model (GLM), which is currently the most common way to analyze fMRI data.

Independent component analysis is a statistical and data-driven technique, which is used for discovering hidden factors from random variables, measurements, and signals. ICA defines a generative model, which is used for source separation or feature extraction from multidimensional data, a large set of samples. The model assumes that observations are produced by linearly mixing some unknown variables [2]. As the name of the method suggests, these variables are assumed to be mutually independent [2]. The ICA attempts to find the set of these independent components and also the linear mixing, which together explain the acquired data. ICA can be seen as an extension of principal component analysis (PCA), but whereas PCA finds the orthogonal vectors and uncorrelated variables, ICA uses higher-order

statistics to unravel independent sources [3].

ICA was first introduced in the early 1980s by Hérault et al. [4] and has thereafter been accepted as a valid analysis tool in different fields of science from engineering to cognitive science. The measured data used for analysis are usually given as a set of parallel signals or time series, which is also the form of fMRI data. During recent years, ICA has been utilized in characterizing fMRI data, and it can used in both spatial and temporal form. Most fMRI studies have used spatial ICA, which finds statistically independent haemodynamic source locations in brain. Thus the independent components represent activations of different brain regions during the measurement. Each component has a separate time course. Temporal ICA can be applied to complete the understanding of the spatiotemporal structure of signal.

ICA's role in fMRI analysis has increased over the last years, as brain studies have evolved towards more naturalistic settings. Unlike the traditional GLM-based approach, ICA does not use any user-specified predictions of expected activations. Thus the method does not require any assumptions or previous knowledge of the relationship between the stimulus sequence and the brain activations, which is a clear advantage when studying brain correlates of complex, unpredictable stimuli. Many possibilities and challenges related to ICA are yet to be discovered; nevertheless, combined with other analysis methods, ICA provides a new tool to gain insight into human brain function.

Chapter 2

Theory

2.1 Human brain

The human brain is a complex organ that consists of neurons, which are the primary functional units in the nervous system, and of glial cells that support neurons and also play a part in signal transmission. The human brain comprises two similar hemispheres. Figure 2.1 shows a rough outline of the major parts of the left hemisphere: the occipital, temporal, parietal and frontal lobes and two main fissures, the Sylvian fissure and the central sulcus. Although the brain accounts only for 2 per cent of body mass, it is very active in energy and oxygen consumption; 20 per cent of body's glucose and oxygen is used in the brain [5].

The outer layer of the brain is called the cerebral cortex, which is a 2–4 millimeter thick [6] layer of gray matter, consisting of the neurons' bodies and dendrites. Beneath the cerebral cortex is the white matter, which consists of myelinated axons of neurons. In addition to structural division, cerebral cortex can also be categorized by its functions, such as visual (see Section 2.1.1) or motor functions.

A neuron is the basic information-processing and -transferring unit in the brain. Figure 2.2 presents the main parts of a neuron. The cell body, called soma, receives signals via dendrites and transmits them to the next neuron through an axon. The major part of cerebral cortex comprises pyramidal cells.

The connection transmitting information between two neurons is called a synapse (see Figure 2.2). When an impulse reaches the end of an axon of the presynaptic cell, transmitter molecules are released to the synaptic cleft and they bind to the receptors in the postsynaptic membrane. The transmission of nerve impulse continues in the neuron through quite locally

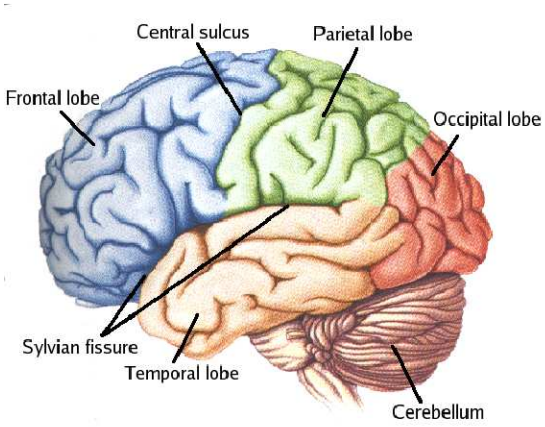

Figure 2.1: The structure of the cerebral cortex of the human brain (modified from [7]).

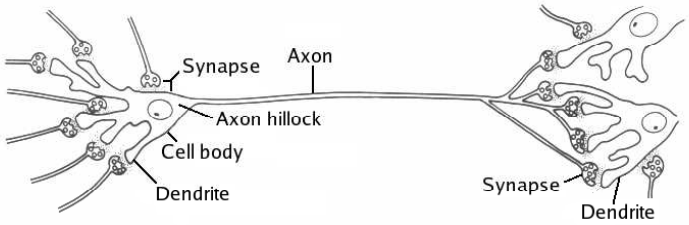

Figure 2.2: The structure of a neuron (modified from [8]).

spreading postsynaptic potentials and propagating action potentials, both related to alterations in membrane potentials.

The release of transmitter molecules and alterations of membrane potential require energy, most of which comes from oxidative metabolism [5]. Thus an activated brain area needs more oxygen, resulting in an increase of blood flow in the vessels of the active region. Also the absolute amounts of oxyhaemoglobin and deoxyhaemoglobin in the blood change. The coupling between neuronal and haemodynamic responses enables the study of human brain function by monitoring blood oxygenation level using fMRI.

2.1.1 Visual cortex

The processing of visual information starts in the retina, which consists of, among others, photoreceptors, bipolar cells and ganglion cells [9]. The central

retina, with densely packed cone cells and sharp central vision, is called the fovea. The information is transmitted to the brain through the optic nerve, consisting of axons of the ganglion cells. Half of the fibres of the optic nerves cross in the optic chiasm, so that the early visual cortex of each hemisphere receives information from the contralateral visual field of both eyes [10]. After the optic chiasm, the transmission of visual information continues in the optic tracts that end in the lateral geniculate nucleus (LGN) in the thalamus. From the thalamus, the information is transmitted to the primary visual cortex V1.

The primary visual cortex is retinotopically arranged. Thus, each part of V1 receives information from a precise part of the visual field, and adjacent points in the visual field are represented in the adjacent areas of V1. The fovea is overrepresented in the cortex so that a large portion of V1 represents the small central portion of the visual field.

In V1, the central vision is represented at the pole of the occipital lobe (see Figure 2.3). The lower part of the visual field is represented above the calcarine sulcus and the upper part below the calcarine sulcus [10]. The greater the distance from the occipital pole, the more peripheral are the corresponding visual field locations.

In addition to V1, the visual information is further processed in visual areas V2, V3, V4, and V5 (also known as MT, middle temporal). These areas are connected with several feedforward and feedback connections. In area V5, the neurons respond to moving visual stimuli in a directionally-selective manner [11].

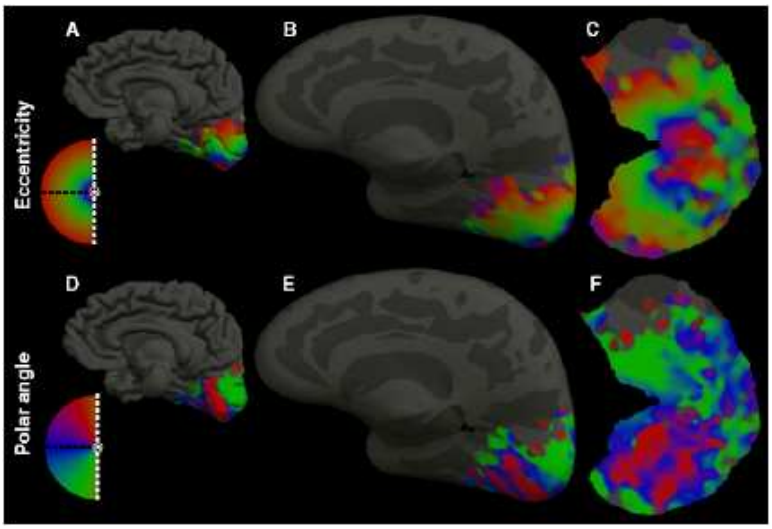

Figure 2.3: Retinotopy of human visual cortex, and isoeccentricity and isopolar angle maps of the human visual cortex. Top: Isoeccentricity coded by color (red [fovea] → blue → green → yellow → red [periphery]) displayed on the original cortical surface (A), on the unfolded cortical surface (B), on and the cut and flattened cortical surface (C). Bottom: Polar angle (red [upper vertical meridian] → blue [horizontal meridian] → green [lower vertical meridian]) plotted on the same three surfaces (D, E, F) (adapted from [12]).

2.2 Magnetic resonance

This section introduces principles of nuclear magnetic resonance and magnetic resonance imaging, that is, the physical phenomena underlying fMRI.

2.2.1 Basics of nuclear magnetic resonance

The protons and neutrons in atom nucleus possess a fundamental quantum mechanical property, termed spin, which can be viewed as an intrinsic angular momentum $\boldsymbol{S}$. According to the rules of quantum mechanics, these angular momenta can only have specific, discrete values, and the number of protons and neutrons in the nucleus determines the possible values of spin angular momentum of a nucleus. The values for the magnitude of $\boldsymbol{S}$ are determined by another fundamental property, the spin quantum number s of a nucleus [1]

$$S = \frac{h}{2\pi}\left[s\left(s+1\right)\right]^{1/2}, \tag{2.1}$$

where h is Planck's constant. For example, hydrogen-1 atom ${}_1H$, which is most commonly used in magnetic resonance imaging, has a nucleus of one proton and a net spin value of 1/2 [1], and thus an intrinsic angular momentum

$$S = \frac{h}{2\pi}\frac{\sqrt{3}}{2}. \tag{2.2}$$

It should be noted that the total angular momentum for atomic or nuclear system has a contribution from orbital motion as well, but in terms of magnetic resonance we can restrict the theory to spin angular momentum.

Because a proton is charged, the rotation of spins also introduces a magnetic moment $\boldsymbol{\mu}$ associated with the intrinsic spin angular momentum [1]. The magnitude of the magnetic moment and the angular momentum vectors are related by [1]

$$\boldsymbol{\mu} = \gamma \boldsymbol{S}, \tag{2.3}$$

where γ is the gyromagnetic ratio of the nucleus; for hydrogen, $\gamma = 42.58$ $\frac{\text{MHz}}{\text{T}}$. The values for the magnitude of the angular momentum $\boldsymbol{S}$, as well as those for the magnitude of the magnetic moment $\boldsymbol{\mu}$, are quantized. For a proton the value is

$$\mu = \frac{\gamma h\sqrt{3}}{4\pi}. \tag{2.4}$$

In the absence of an external magnetic field, the individual magnetic moments are randomly oriented. Two discrete values are found for any measurement of a given spin component. In an external magnetic field B_0, oriented parallel to the z axis, μ_z can only have values given by [1]

$$\mu_z = \gamma S_z = \frac{\gamma h}{2\pi} m_l, \tag{2.5}$$

where m_l is the nuclear magnetic quantum number, which can have values $m_l = s, s-1, ..., -s$. For proton, this means $m_l = \pm 1/2$ and the possible values for μ_z are $\pm\frac{\gamma h}{4\pi}$.

Thus in an external magnetic field the protons' magnetic moments have two possible orientations; the nuclear magnetic moment can be aligned either parallel or opposite to the external field as shown in Figure 2.4 (left).

As discussed earlier, in the absence of a magnetic field, only one energy state is possible, but in an external magnetic field the Zeeman splitting causes the energy state to split into two possible energy states. The parallel orientation of magnetic moment corresponds to the lower energy state, and the anti-parallel orientation to the higher energy state. Figure 2.4 (right) shows the splitting of the energy states.

Interaction energy of a magnetic moment with the external field is given by [1]

$$E = -\mu_z B_0 = \pm\frac{\gamma h B_0}{4\pi}, \tag{2.6}$$

leading to an energy difference between the two states

$$\Delta E = \frac{\gamma h B_0}{2\pi}. \tag{2.7}$$

In an equilibrium state the system minimizes its free energy, and due to thermal excitations there are spins on both energy states. The relative number of protons in the two energy states is derived from Boltzmann statistics: in a magnetic field of 3 T and room temperature, for every million protons the population difference between parallel and antiparallel orientations is approximately 10 protons [1]. The configuration can be changed by exciting individual spins from lower energy state to the higher.

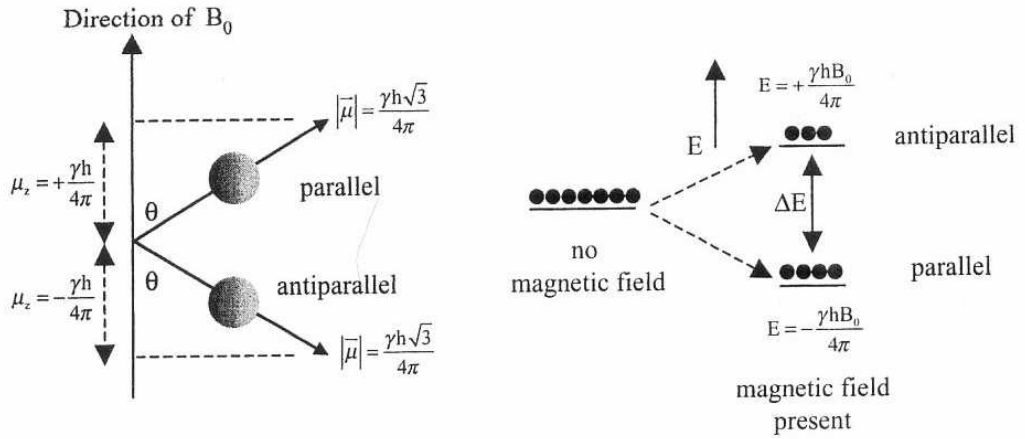

Figure 2.4: Left: The magnetic moments of protons can align either parallel or opposite to the external magnetic field. The angle θ between the direction of the field and magnetic moment is 54.7°. Right: The energy states corresponding to antiparallel and parallel configurations (modified from [1]).

The energy needed for excitations from lower to higher energy states comes from electromagnetic radiation, applied as a pulsating magnetic field B_1 orthogonal to B_0. The energy gap between the energy states, as described in Equation 2.7, determines the angular frequency of pulsation ω_1 of B_1

$$hf_1 = \Delta E = \frac{\gamma h B_0}{2\pi}, \tag{2.8}$$

$$\omega_1 = 2\pi f_1 = \gamma B_0. \tag{2.9}$$

Thus, the application of the pulsating magnetic field results in a non-Boltzmann distribution of the populations in the parallel and antiparallel states [1].

As shown previously, the nuclear magnetic resonance phenomenon is based on complex quantum mechanics. However, as magnetic resonance imaging is based on observing a large amount of nuclei in a macroscopic sample, we can continue the study of interactions in terms of classical mechanics.

The angle between the magnetic moment of proton $\boldsymbol{\mu}$ and the external magnetic field $\boldsymbol{B_0}$ is $\theta = 54.7°$ as presented in Figure 2.4 [1]. The magnetic field attempts to align the magnetic moment parallel to its direction, which results in a torque. The torque makes the magnetic moments precess around the external field, keeping the constant angle θ between $\boldsymbol{\mu}$ and $\boldsymbol{B}_0$. The frequency of precession is [1]

$$\omega_{\text{prec}} = \gamma B_0, \tag{2.10}$$

hence the angular frequency of the precession of the magnetic moment is proportional to the magnitude of the external field. This frequency is called the Larmor frequency. The frequency ω_1 of the applied electromagnetic field (Eq. 2.9) needed to induce the excitations is identical to the Larmor precession frequency ω_{prec}. In a 3-T magnetic field the Larmor frequency of hydrogen atom is approximately 128 MHz, which is in the radiofrequency (RF) range.

The net magnetization $\boldsymbol{M}$, which is a vector sum of individual proton magnetic moments, has in the equilibrium only a z-component, as the x- and y-components of individual magnetic moments cancel out, see Figure 2.5. The magnetic moments precess about the z-axis and produce a longitudinal magnetization $M_z = M_0$. To create a signal detected with a coil, the magnetization vector needs to be rotated towards the xy plane to create the M_x and M_y components. If we apply another magnetic field perpendicular to the original magnetic field, it again creates a torque, which rotates the magnetization vector toward the xy plane. Figure 2.6 presents the process.

The magnetic field $\boldsymbol{B}_1$, applied along the x axis, pulsates at Larmor frequency $\omega_{\text{prec}} = \omega_1$ and transfers energy to protons. As the individual magnetic moments continue precessing at the Larmor frequency about the main magnetic field, also the magnetization vector $\boldsymbol{M}$ precesses in the xy plane.

In Figure 2.6, the magnetization vector is rotated by 90° into the xy plane, but also other flip angles can be used in NMR imaging. The angle

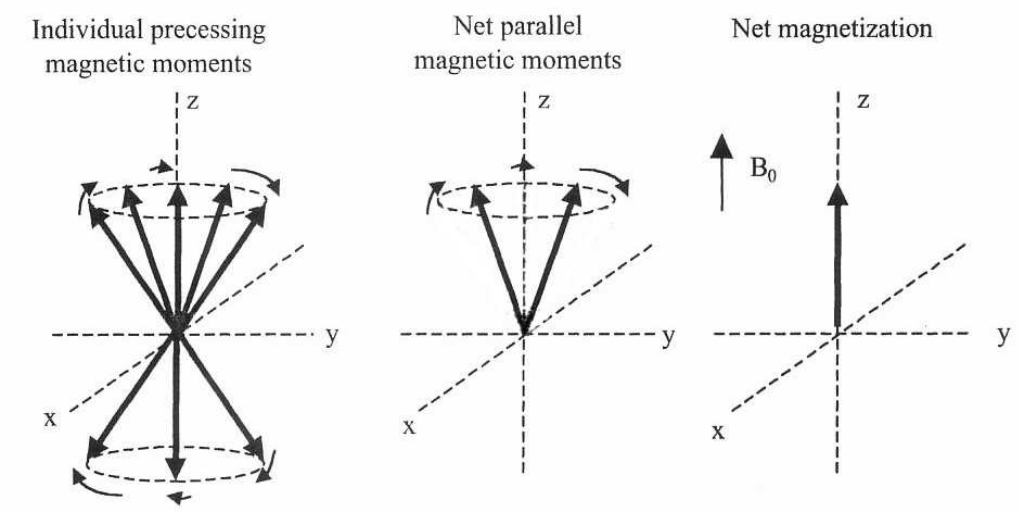

Figure 2.5: Individual magnetic moments precess about the external magnetic field. There are slightly more spins with parallel orientation, which results in a static net magnetization in the z direction (modified from [1]).

through which the magnetic moments are rotated is determined by [1]

$$\alpha = \gamma B_1 \tau_{B_1}, \tag{2.11}$$

where τ_{B_1} is the time for which the pulsating field is applied.

In the vector model, this means that the original magnetization vector M_0 in z direction is reduced and the M_x and M_y components have non-zero values. After some time, when the RF field has been switched off, the magnetic moments restore their equilibrium distribution and the net magnetization is again aligned in the z direction.

2.2.2 T1 relaxation

The return of M_z to its equilibrium value is called T1 relaxation. The magnitude of this component can be calculated from Bloch equations [5] and it takes a form

$$M_z = M_0 \cos\alpha + (M_0 - M_0 \cos\alpha)\left(1 - e^{-\frac{t}{T1}}\right), \tag{2.12}$$

where α is the flip angle and t is the time after the RF pulse. Relaxation time constant T1 is the time during which the longitudinal component (the component in z-direction) of net magnetization vector reaches the value $M_z = M_0(1 - e^{-1})$, i.e., restores 63% of its original value. After applying the

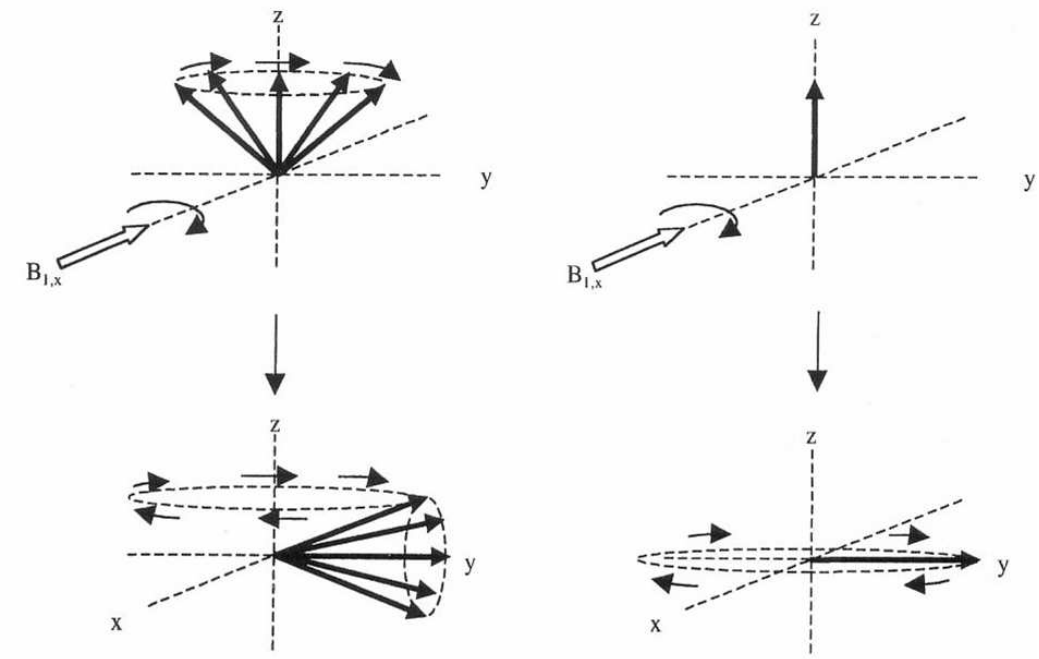

Figure 2.6: Precessing magnetic moments result in a net magnetization in the direction of the z-axis. When a pulsating magnetic field $\boldsymbol{B}_{1,x}$ is applied in the direction of the x-axis, the magnetization is turned towards the xy plane, where the precession continues at the Larmor frequency (modified from [1]).

RF pulse, the thermal processes return the individual spins to the equilibrium distribution, and thus also the net magnetization restores its original state. The magnetic field experienced by spin depends not only on the external fields, but also on the magnetic moments and fluctuations of its neighbouring spins [5]. T1 relaxation depends on the strength of Larmor frequency component of this randomly fluctuating magnetic field. T1 relaxation is also called spin-lattice relaxation as this process involves energy transfer between the proton spin and lattice phonons. Different tissues have different values of relaxation time constants, which forms the basis for separating tissues in MR image.

2.2.3 T2 and T2* relaxation

The return of M_x and M_y to their equilibrium values after the RF pulse is defined by T2 relaxation time constant. The Bloch equations give for the decay of transverse magnetization [5]

$$M_{xy} = M_0 \sin(\alpha) e^{-t/T2}, \tag{2.13}$$

where α is again the flip angle and t time after a RF pulse. T2 relaxation involves the loss of "phase coherence" between the protons precessing in the transverse plane [5]. Even if the magnetic field $\boldsymbol{B}_0$ is perfectly homogeneous, variations in the interactions between neighboring nuclei exist causing the Larmor frequencies of different nuclei to vary. As a result these slight decreases or increases in the Larmor frequency lead to decrease in net transverse magnetization over time [5]. Finally, when the individual magnetic moment vectors are randomly distributed in the transverse xy plane, there is no net magnetization M_{xy} or signal to be detected.

In addition to the process described above, a second mechanism causes the loss of phase coherence and signal in transverse plain, called T2* relaxation. This phenomenon arises from the spatial variations in the strength of the magnetic field within the body [5]. One source for these variations is the external magnetic field; it is not possible to produce a totally homogeneous magnetic field. The second source is local variations in the magnetic field due to minor local differences in chemical environments and different magnetic susceptibilities in different regions of the body, for example in different tissues.

Thus T2* is influenced by the field inhomogeneities and is always shorter than T2. The relationship between these two relaxation times comes from

$$\frac{1}{T2^*} = \frac{1}{T2} + \frac{1}{T2'}, \tag{2.14}$$

where $T2'$ is spin dephasing due to field inhomogeneities.

2.3 Magnetic resonance imaging (MRI)

2.3.1 MRI scanner

Figure 2.7 shows a schematic configuration of an MRI scanner. The external static and homogeneous magnetic field $\boldsymbol{B}_0$ is in modern high-field scanners typically produced with a superconducting magnet. The RF coil is used for generating the magnetic field $\boldsymbol{B_1}$ pulsating at Larmor frequency. Signal is detected either with the same or a separate coil. After the RF pulse, the precessing, time-varying magnetization vector produces a time-varying magnetic field, which induces voltage into the RF coil [1]. According to the law of induction, only a changing magnetic flux can induce voltage to a current loop, and thus at equilibrium the static magnetization vector does not induce voltage to the loop. The frequency and phase of the precessing magnetization vector are measured with the RF coil and an inverse two-dimensional Fourier transform over the imaging sequence is calculated to

produce the image in spatial domain. The image formation is described in more detail below.

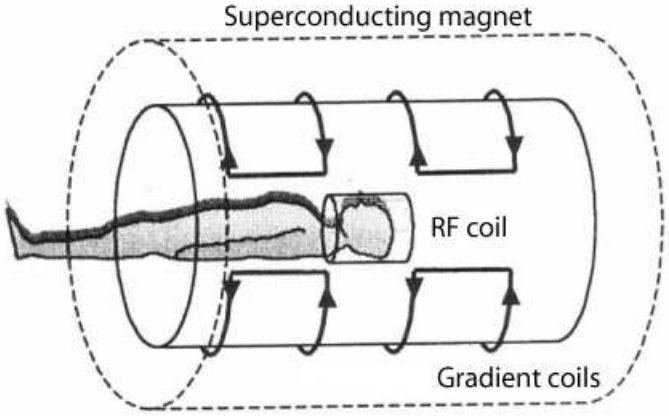

Figure 2.7: The main hardware of the MRI scanner (modified from [1]).

2.3.2 Image formation

Forming an image of a certain part of the body requires a way of distinguishing the signals coming from its different parts. Magnetic resonance imaging is based on encoding the spatial information using magnetic field gradients [5]. The gradient coils impose a linear variation in the external field $\boldsymbol{B}_0$ in all three dimensions, creating linear dependence in Larmor frequencies upon the spatial locations of the protons. Compared with the static field $\boldsymbol{B}_0$, gradient coils provide smaller, rapidly changing magnetic fields [1].

Spatial variations are induced in the volume of interest, so that resonance frequency ω_{prec} of nucleus contains information of its location. The gradients are imposed to the main magnetic field $\boldsymbol{B}_0$, which is again assumed to be aligned in the z-direction, in three spatial dimensions:

$$\frac{\partial B_z}{\partial z} = G_z \tag{2.15a}$$

$$\frac{\partial B_z}{\partial x} = G_x \tag{2.15b}$$

$$\frac{\partial B_z}{\partial y} = G_y. \tag{2.15c}$$

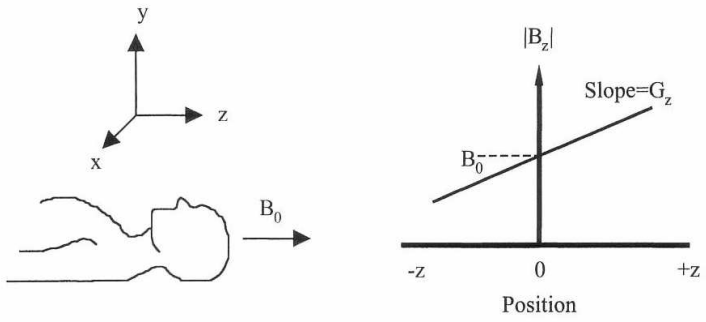

Figure 2.8: Left: The coordinate system and direction of static magnetic field. Right: The dependence of the magnetic field strength on the spatial coordinate z (modified from [1]).

In the presence of a gradient in z-direction, as shown in Figure 2.8, all the protons in an xy-plane, defined by a common coordinate z, experience a field

$$B_z = B_0 + zG_z, \tag{2.16}$$

and the corresponding precession frequencies of protons are dependent on their location as

$$\omega_{\text{prec,z}} = \gamma(B_0 + zG_z). \tag{2.17}$$

Similar dependence of location can also be produced in x and y directions.

The image formation includes three stages: slice selection, phase-encoding and frequency-encoding [1]. The type and quality of the acquired images depend on the use of the three gradient directions during these three stages. Usually the image is formed by a pack of slices, with desired thickness and orientation. In other words, the 3-D object is divided into 2-D slices and the image of each slice is formed separately.

Slice selection includes application of the RF pulse simultaneously with a selected gradient direction, which is normal to the desired plane. Based on Equation 2.17, the frequency of RF pulse determines the spins which are excited. Figure 2.9 shows the three possibilities of spatial gradients, or their combination, which results in an oblique slice angle [1]. Here we use the slice selection gradient in the z direction.

The thickness and position of a slice are determined by the applied frequency ω_s and the bandwidth of excitation. The ideal shape of the frequency response is a box-shaped function, shown in Figure 2.10, and thus the shape of RF signal is its Fourier transform, a sinc-shaped function [13]. When this sinc-modulated RF pulse is applied at the same time with the field gradient

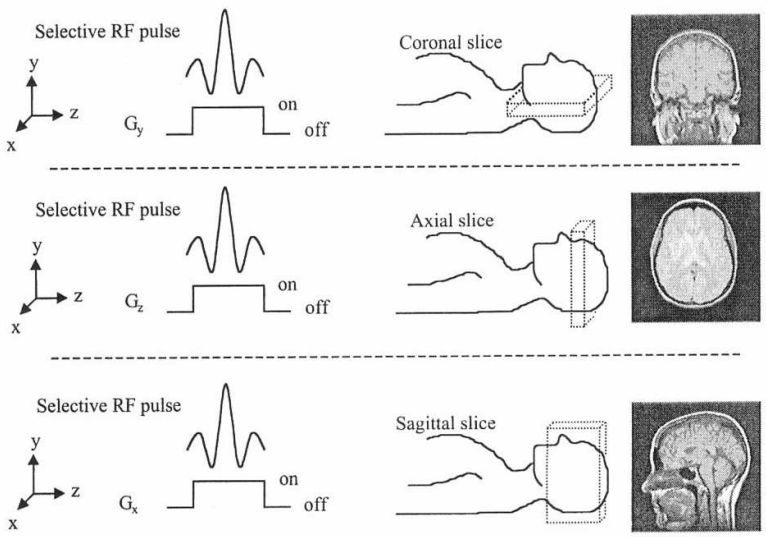

Figure 2.9: The slice selection using the three different gradients in y, z or x direction. These produce a pack of coronal, axial or sagittal slices, respectively (modified from [1]).

in z direction, the protons with Larmor frequency between $\omega_s - \Delta\omega_s$ and $\omega_s + \Delta\omega_s$ are excited.

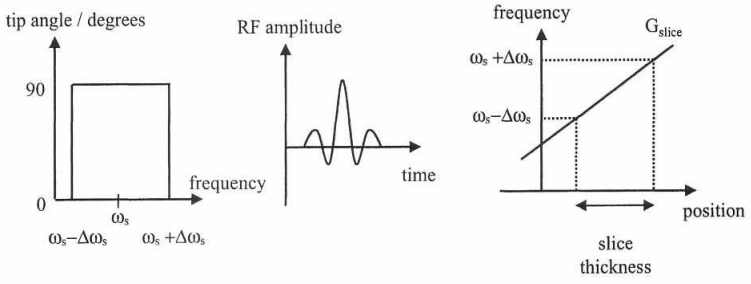

Figure 2.10: Left: Frequency response of RF pulse that excites the spins with Larmor frequencies in the range $[\omega_s - \Delta\omega_s, \omega_s + \Delta\omega_s]$. Center: Shape of the RF pulse. Right: Slice selection (modified from [1]).

A 2-D image of the plane defined by slice selection is formed by using the two free gradient directions, namely x and y. The goal is to determine the spin density on the given slice as a function of spatial coordinates by measuring the signal produced by excited spins. This is possible, as the frequency variations imposed by gradients into the spins contain information about the spatial distribution of the spins [13]. This type of imaging is called

Fourier imaging.

The Larmor frequency for a proton in an arbitrary location on the chosen plane can be written as

$$\omega_{\text{prec}}(x, y) = \gamma (B_0 + G_x x + G_y y). \tag{2.18}$$

Thus after the excitation pulse, the tipped magnetization vector starts to gain a phase

$$\varphi(x, y, t) = \omega_{\text{prec}}(x, y)\, t, \tag{2.19}$$

where t is time after excitation.

The signal that is acquired over the whole plane at different time instances t can be written as an integral over the slice. The real and imaginary parts of the signal separate the contributions along the x and y axes. The signal strength is proportional to the density of spins $\rho(x, y)$ and as we are interested in the effect of different gradients to the signal, we can leave the static term $\boldsymbol{B}_0$ out. Then equation for measured signal $S(x, y)$ takes the form

$$S(t) = \int\int \rho(x, y) \{\cos[2\pi\gamma t (G_x x + G_y y)] + i \sin[2\pi\gamma t (G_x x + G_y y)]\}\, dxdy. \tag{2.20}$$

With change of variables we define k_x and k_y as

$$k_x = 2\pi\gamma G_x t \tag{2.21a}$$

$$k_y = 2\pi\gamma G_y t. \tag{2.21b}$$

Now we can simplify Equation 2.20

$$S(k_x, k_y) = \int\int \rho(x, y) \exp^{i(k_x x + k_y y)}\, dxdy. \tag{2.22}$$

The signal is now the 2-D inverse Fourier transform of the spin density, which means that using Fourier transform we can obtain the distribution of the spins on the selected slice as

$$\rho(x, y) = \int\int S(k_x, k_y) \exp^{i(x k_x - y k_y)}\, dk_x dk_y. \tag{2.23}$$

This means that if we collect all the points in the $k_x k_y$-space, we can reconstruct the image, as shown in Figure 2.11. That can be done by measuring the signal S when changing the values for k_x and k_y, i.e., the gradients in x and y directions.

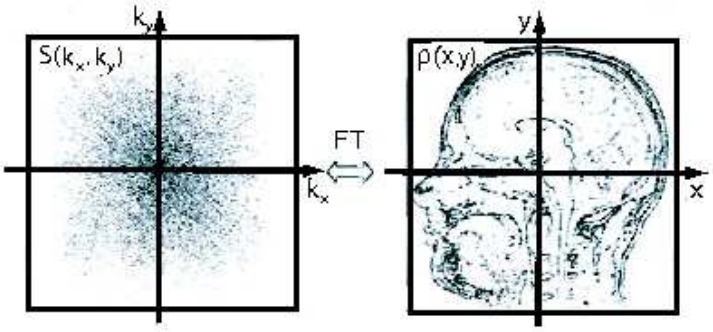

Figure 2.11: The Fourier transform enables the reconstruction of image after sampling of k-space (modified from [5]).

In practise, the Fourier imaging is implemented by turning the two gradients, called phase-encoding gradient G_{phase} and frequency-encoding gradient G_{freq}, on and off. Figure 2.12 shows a basic imaging sequence for forming an image of one slice. After application of the RF pulse, G_{phase} is used before and G_{freq} during the data acquisition. The phase-encoding gradient imposes spatially dependent phase shift, which is also proportional to the strength of the gradient. Next, frequency-encoding gradient is applied and the values are read from the nuclei precessing in different frequencies, number of point in this direction is N_r. The reading process is repeated for each different value of phase (in total N_p values) until the whole k-space is read. Thus for one slice total of $N_p \times N_r$ data points are acquired.

2.3.3 Spin-echo imaging sequences

Spin-echo imaging sequence is based on application of two RF pulses. The advantage of spin-echo sequence is that the the second RF pulse refocuses the effect of $T2'$, which means that the loss of transverse magnetisation and the signal detected is mainly due to T2.

The first RF pulse is applied as in Figure 2.6 at $t = 0$. The magnetic field pulsates in the x direction and the magnetization vector is rotated onto the transverse plane, aligned with y axis. The different spins start to accumulate different phases due to experiencing slightly different magnetic fields. Another RF pulse, twice the magnitude is applied along y axis after time τ. This pulse inverts the phases that the spins have gained and the spins rephase, so that at the time instance $t = 2\tau = \mathrm{TE}$ (time to echo), the spins are again aligned in the y direction. This realignment is called a spin-echo.

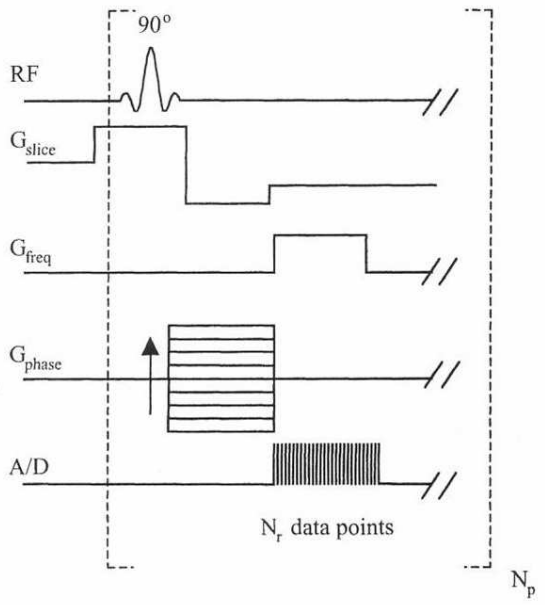

Figure 2.12: Basic example of an imaging sequence including spin excitation (RF pulse), slice selection (G_{slice}), phase encoding (G_{phase}) and frequency encoding (G_{freq} for reading). The sequence is repeated N_p times and each time N_r data points are read. The oscillating voltage signal is digitized using A/D converter (modified from [1]).

The signal is collected after spin-echo and then the loss of magnetization is only due to T2 processes.

The TE presented above is called echo time. TE is twice the duration of τ, which is the time between the first and second RF pulses. TR is the repetition time, the time between the spin-echo sequences. The values for TR and TE define how T1 and T2 contrasts are weighted in the image.

2.3.4 Gradient-echo imaging sequence and EPI

When fast imaging times are required, spin-echo sequences are not optimal, since they require long TR. Moreover, they are not optimal if one is interested in quantifying the susceptibility changes [1]. Gradient-echo sequences do not use refocusing pulses, but instead dephasing and rephasing gradients to create an echo, and thus shorter TE and TR values can be applied. To image rapidly, the tip angle of the RF pulse is reduced to value much smaller than 90°. Several variations of gradient-echo sequence, such as fast low-angle shot (FLASH) or spoiled gradient-recalled (SPGR), can be used for anatomical

brain images and for echo-planar imaging (EPI) sequences that are utilized in functional imaging of the brain.

Blood oxygenation level-dependent (BOLD) fMRI is usually achieved with gradient-echo sequence EPI (see Figure 2.13), which is one of the most efficient MRI techniques. The use of a contrast dependent on blood oxygenation was discovered by Ogawa et al [14]. Echo-planar imaging achieves its speed by obtaining an image after a single RF excitation. The faster scans help to reduce motion-related artifacts in MR images and they also improve the temporal resolution. Again there are also some restrictions to echo-planar imaging. As the signal is decaying with the time constant $T2^*$ during acquisition, a limited number of data points can be collected on k space, causing the pixel-resolution to decrease. The rapidly changing magnetic field gradients can also cause nerve stimulation and the acoustic noise can be disturbing.

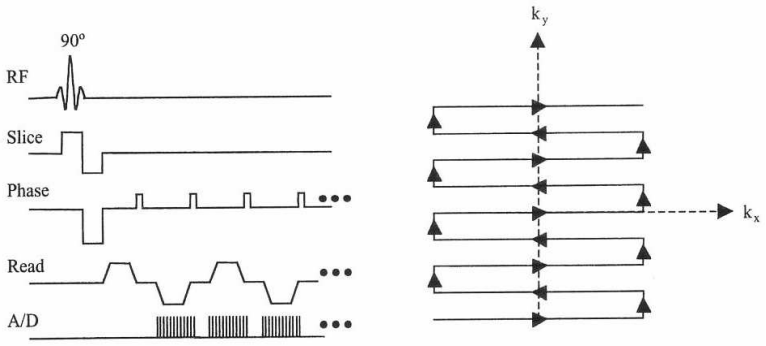

Figure 2.13: Left: Basic EPI sequence, where the data for the whole slice are acquired after one excitation pulse. Right: The points are collected in the k space one line at the time (modified from [1]).

2.4 BOLD

FMRI is based on measuring haemodynamic changes in the brain. Two main fMRI methods are the perfusion fMRI, which is based on measuring the local changes in blood volume, and blood-oxygenation-level-dependent (BOLD) fMRI, which is the most commonly used fMRI method and also applied in this study.

The basis of BOLD is the change of blood oxygenation level during activation of a brain region. When the blood oxygen level increases, the BOLD signal increases as well. The susceptibility reflects the deoxyhaemoglobin levels,

and blood flow and cerebral oxygen utilization affect the deoxyhaemoglobin levels [13]. Oxyhaemoglobin is diamagnetic, while deoxyhaemoglobin is paramagnetic and, thus, a change in haemoglobin oxygenation level changes the local magnetic susceptibility. In external magnetic field $\boldsymbol{B}_0$, neuronal activation results in local variation in the field and slightly different Larmor frequencies of neighbouring nuclei. The $T2^*$ relaxation, as discussed earlier in Section 2.2.3, is based on local variations in magnetic field caused by different magnetic susceptibilities. Thus in BOLD fMRI $T2^*$-weighted imaging is used.

Chapter 3

Methods

3.1 Stimuli

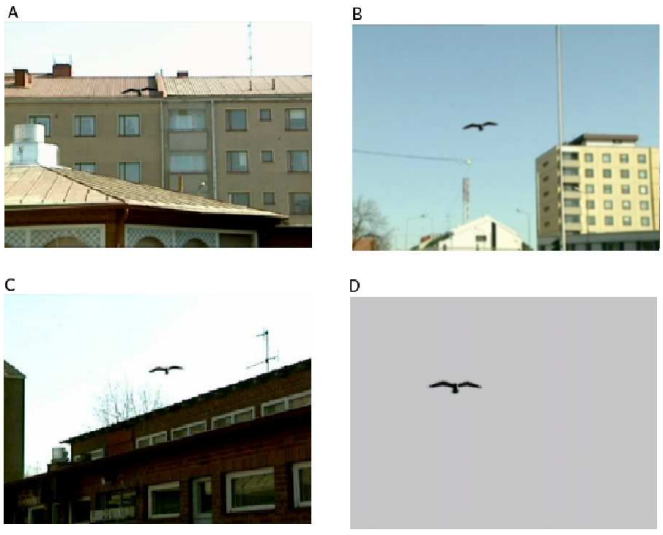

Figure 3.1: Examples of stimuli used in this study. A, B and C are examples of condition with different backgrounds. D presents a condition with no background.

The stimulus sequence consisted of four different types of video stimuli, all with an animated bird (see Figure 3.1). The background of the stimulus was either a natural environment with trees, houses, streets etc. (NAT) (Figures 3.1 A–C) or plain gray (GRAY) (Figure 3.1D). The bird was either staying still (STILL) or gliding smoothly across a random path over the background

(MOVE). The subject's task was to follow the bird with gaze. During the rest condition, the subject fixated a black cross on a gray background in the center of the screen.

Figure 3.2 presents the whole stimulus sequence. The videos lasted for 6–60 s, alternating with 20-s rest periods. One stimulus session lasted for 10 min 47 s. The stimulus sequence was presented with Presentation 9.70 software [15]. The videos were projected on a transparent screen, and the subjects viewed them via a mirror. The screen size was 20 ×15 cm^2 and the viewing distance 35 cm. The resolution of the videos was 640 × 480 pixels. The stimulus sequence was presented two times for each subject.

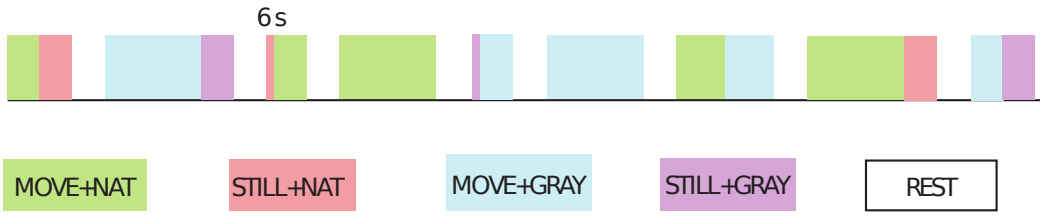

Figure 3.2: The order of the stimulus blocks within the sequence (total duration 10 min 47 s); the shortest block length of 6 s indicated at the top.

3.2 Subjects

We measured 9 healthy volunteers (3 female, 6 male), mean age 27 years, range 22–32 yrs. One subject had to be excluded from data analysis due to movement artifacts, so that the following results are for 8 subjects. All subjects gave their written informed consent and filled in a safety screening form. The study had a prior approval by the Ethics Committee of the Hospital District of Helsinki and Uusimaa.

3.3 Imaging

The fMRI data were acquired using a Signa VH/i 3.0T MRI scanner (General Electric, Milwaukee, WI) while the subject's head was positioned in an 8-channel head coil. Images of functional sessions were acquired using T2*-weighted EPI sequences (TR = 3000 ms, TE = 32 ms, flip angle = 90, 64 × 64 matrix, field of view 20 × 20 cm^2). The brain ("volume") was covered with 44 slices (thickness 3 mm), parallel to commissural axes. The total duration of the measurement was 2 × 216 × 3 s = 1290 s.

Whole-head anatomical T1-weighted three-dimensional spoiled gradient-recalled (3D-SPGR) images were also acquired (256 × 256 matrix, field of view 24 × 24 cm^2, slice thickness 1 mm, number of slices 154).

3.4 Eye tracking

In this experiment, we also monitored subjects' eye gaze with SMI MEye Track long-range eye-tracking system (Sensomotoric Instruments GmbH, Germany); iViewX software from the same company for acquiring the data.

The camera was placed to the mount at the end of the bed and mirror-box on top of the head-coil, as shown in Figure 3.3. One eye was tracked by illuminating the eye with infrared light attached to the mirror box. The Presentation-software script was modified to control the eye-tracking system, so that the eye-tracking data (i.e., coordinates of the fixation sites of the eye) could later be synchronized with the measured fMRI data and the stimulus sequence. The sampling rate of the recording was 50 Hz.

A Matlab programme by M.Sc. (Tech.) Veli-Matti Saarinen (Brain Research Unit at Aalto University) enabled the combination of the recorded eye-tracking data and video stimuli to show the focus of the vision during measurement. Figure 3.4 present the programme interface.

Saarinen also analyzed the movement of the focus of the gaze during STILL condition, when the subject was supposed to fixate the still bird.

At that time of our measurement, the eye-tracking system was still under testing, and we were able to perform this analysis only for three subjects. The development of the eye-tracking systems has continued since this experiment and in the future, with even more real-world-like set-ups, the eye-tracking will provide interesting information about the subject's behaviour and focus of attention.

Figure 3.3: SMI eye-tracking system implemented in the MRI environment at the AMI center.

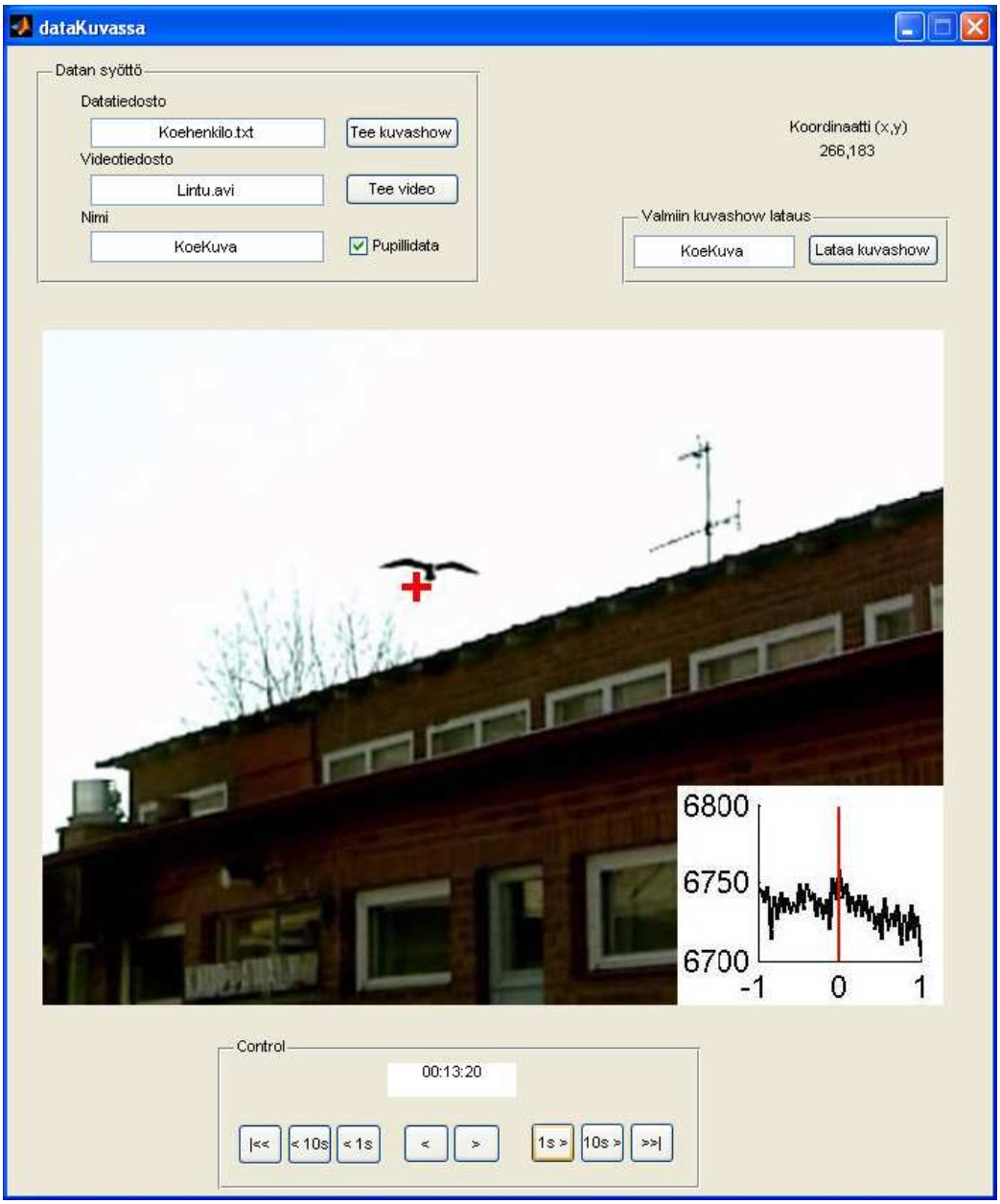

Figure 3.4: User interface of the Matlab programme that presents the focus of the vision with red cross. The box in the lower right hand corner presents the behaviour of the pupil size in arbitrary units as a function of time, from –1 to +1 seconds. Courtesy of Veli-Matti Saarinen, BRU, Aalto University.

Chapter 4

Analysis of fMRI data

4.1 Preprocessing with SPM2

The DICOM (The Digital Imaging and Communications in Medicine) images acquired from the MRI measurements were first transformed to analyze format using MRIcro software [16]. Preprocessing of the data continued with the Matlab SPM2 software package [17]. The spatial preprocessing included realignment, coregistration, normalization and spatial smoothing.

4.1.1 Realignment

Realignment corrects the subject's movements from the time series; due to the head movements, voxels in the subsequent volumes may not represent the same brain area. Thus, a correction is necessary for the following voxel-based analysis, which assumes all data of a particular voxel to be derived from the same part of the brain. All volumes of a session were aligned so that the data were spatially matched with the reference scan, in this case with the first volume of a time series.

Realignment begins with estimation of 6 parameters (3 for translation, 3 for rotation) with an affine transformation to minimize the sum of squared differences between each successive scan and a reference scan [18]. Thereafter, the transformation is applied by re-sampling the data using an interpolation method; we used the SPM2 default setting, that is the 4th degree B-spline method. The re-sampling can also be done after normalization, as was done in our study.

4.1.2 Coregistration of functional and structural data

Coregistration aligns the functional data with the same subject's structural images; this procedure is necessary for visualization of the functional data. For coregistration, we calculated a mean image using the EPI files of the first of the two sessions, and this mean functional image was coregistered to skull-stripped anatomical image [19]. We then applied in SPM within-subject registration using normalized mutual information algorithm determined with six parameters [18].

4.1.3 Normalization

Group analysis of functional data requires inter-subject averaging. Thus every subject's functional images have to be spatially normalized into a standard space. First, the anatomical image of a subject was mapped on a template image and an algorithm was used to estimate a 12-parameter affine transformation to correct for the variation in position and size of the image. Nonlinear transformations were performed to correct more subtle differences. The estimated parameters were then applied to all subjects' functional images. We used template image of the Montreal Neurological Institute (MNI) space, which is constructed from skull-stripped anatomical brain images of 152 subjects; it resembles closely the Talairach space [20].

4.1.4 Spatial smoothing

Spatial smoothing replaces the intensity value within each voxel with a weighted average of intensity values of neighbouring voxels. The choice of filter is determined by the matched-filter theorem, which states that the filter that gives the optimum resolution of signal to noise is the one that is matched to signal, i.e., the filter has to be matched to the size of the activation we wish to detect.

Individuals' structural and functional brain data differ, so that the activation points can be expected to be widely distributed over the cortical surface. Thus it is wiser to use a wide smoothing to detect a signal on a group level, and the full-width-half-maximum (FWHM) is usually chosen to 2–3 times the voxel size. After smoothing, the data also conform more accurately to a gaussian random field theory, which is used in statistical voxel-by-voxel analysis. In this study, the voxel size was 3 mm and spatial smoothing was performed with a 6-mm FWHM gaussian filter.

4.2 Analysis based on the general linear model (GLM)

The general linear model can be used in a wide variety of statistical analyses and can be considered as an extension of linear multiple regression. GLM assesses the relations between dependent variable and independent, explanatory variables. General linear model implemented in SPM is based on voxel-by-voxel testing, and the goal of GLM analysis in brain studies is to identify regions that show a statistically significant experimental effect of interest [21].

In GLM analysis, we want to estimate a linear equation of the form

$$\boldsymbol{Y} = \boldsymbol{X}\boldsymbol{b} + \boldsymbol{e}, \tag{4.1}$$

where $\boldsymbol{Y}$ includes the values for dependent variable, i.e. the measured data, $\boldsymbol{X}$ the values for independent variables, i.e., our model, and $\boldsymbol{b}$ includes the regression coefficients, which represent the independent contribution of each independent variable to the prediction of the dependent variable. In vector $\boldsymbol{e}$, we have the residual values and the goal of multiple regression is to minimize the sum of squared residuals.

We can have N observed values in $\boldsymbol{Y}$, for example time series for one voxel and L independent variables. Thus Equation 4.1 can be written in a form

$$\begin{bmatrix} Y_1 \\ Y_2 \\ . \\ . \\ Y_N \end{bmatrix} = \begin{bmatrix} X_{11} & X_{12} & . & . & X_{1L} \\ X_{21} & X_{22} & . & . & X_{2L} \\ . & . & . & . & . \\ . & . & . & . & . \\ X_{N1} & X_{N2} & . & . & X_{NL} \end{bmatrix} \begin{bmatrix} b_1 \\ b_2 \\ . \\ . \\ b_L \end{bmatrix} + \begin{bmatrix} e_1 \\ e_2 \\ . \\ . \\ e_N \end{bmatrix}. \tag{4.2}$$

The matrix $\boldsymbol{X}$ that contains the explanatory variables is called the design matrix [21]. Each row in the design matrix corresponds to one time point of the measured data, the columns correspond to the explanatory variables or regressors of the model. The residual errors are assumed to be identically and normally distributed [21].

In the general linear model of SPM, the parameter estimates $\hat{\beta}$ are determined by minimizing the squared residuals

$$S = \sum_{j=1}^{N} e_j^2 = \boldsymbol{e}^{\mathbf{T}}\boldsymbol{e} = \sum_{j=1}^{N} \left(Y_j - X_{j1}\hat{\beta}_1 - ... - X_{jL}\hat{\beta}_L \right)^2. \tag{4.3}$$

This function is minimized when its first derivative with respect to $\hat{\beta}$ is zero, that is

$$\frac{\partial S}{\partial \hat{\beta}_l} = 2\sum_{j=1}^{N}(-X_{jl})\left(Y_j - X_{j1}\hat{\beta}_1 - ... - X_{jL}\hat{\beta}_L\right) = 0. \tag{4.4}$$

The right side of the Equation 4.4 is the l^{th} row of matrix equation $\boldsymbol{X^T Y} = \left(\boldsymbol{X^T X}\right)\hat{\boldsymbol{\beta}}$. The parameter estimates are the least squares estimates (LSE) derived from $\hat{\beta} = \left(\boldsymbol{X^T X}\right)^{-1}\boldsymbol{X^T Y}$. If the errors are normally distributed, the least-squares estimates are the maximum likelihood estimates (MLE) and the best linear unbiased estimates. SPM2 uses Restricted Maximum Likelihood (ReML) estimates, which allow departures from distribution assumptions. The unbiasedness criterion requires that the expected value of $\hat{\beta}$ is β, i.e., $E\left\{\hat{\beta}\right\} = \beta$.

Here we have to note that the inverse matrix exists only if matrix $\mathbf{X}$ is full rank, i.e., the explanatory variables are linearly independent. This is not always the case, especially in a small data set two explanatory values can be perfectly correlated, and thus we use pseudoinverse instead[21].

In fMRI scanning, the dependent variable $\boldsymbol{Y}$ is a single voxel's time-series. The independent variables in $\boldsymbol{X}$ come usually from stimulus conditions, and the matrix is formed based on stimulus blocks and convolved with the haemodynamic response function.

The voxel-by-voxel analysis continues with statistical t-test. We want to find out if there is an effect of interest after other modelled effects have been taken into account. The parameter estimates are normally distributed $\hat{\beta} \sim N(\beta, \sigma^2(\boldsymbol{X}^{\mathrm{T}}\boldsymbol{X})^{-1})$ and we can study different contrasts of parameter estimates using a linear combination of the parameters. For a linear combination, it holds that $c^{\mathrm{T}}\hat{\beta} \sim N(c^{\mathrm{T}}\beta, \sigma^2 c^{\mathrm{T}}(\boldsymbol{X}^{\mathrm{T}}\boldsymbol{X})^{-1}c)$. The value of test statistic t is the contrast of estimated parameters divided by the square root of variance estimate

$$t = \frac{\boldsymbol{c^T}\hat{\beta}}{\hat{std}\left(\boldsymbol{c^T}\hat{\beta}\right)}. \tag{4.5}$$

The null hypothesis is that the product $\boldsymbol{c^T}\hat{\beta}$ is zero. The p-value then gives the probability of obtaining the value for test statistic t given that the null hypothesis is true.

We analyzed the fMRI data using the GLM-based analysis inbuilt in SPM2 [17]. First the data of each subject were analyzed separately. Four explanatory variables, one for each condition, were introduced as boxcar functions determined by stimulus onset and offset times, convolved with the

haemodynamic response function. Contrast images for each subject were defined to represent the effects of different conditions. A high-pass filter with a cut-off at 1/460 s removed low-frequency noise, and serial correlations were accounted for with an AR(1) model.

When multiple statistical tests are being performed simultaneously, the probability of false positives increases. In voxel-by-voxel analysis, the number of statistical tests is over a hundred thousand, and correction for multiple comparisons is needed. SPM includes corrections based on controlling either the family-wise error or false discovery rate [21]. It is also possible to set an uncorrected threshold.

T-test parametric maps of each condition were generated for each subject. In fMRI studies, we often want to make statistical inferences from the data of many subjects, that is to study the population effect. Commonly used is random-effects analysis, which takes into account both within- and between-subject variabilities [21]. In our study, group analysis was performed using one-sample t-test and random-effects analysis. We compared the four stimulus conditions with the statistical threshold set to $p < 0.001$ (uncorrected) and the minimum value of 20 activated voxels in a cluster.

4.3 Independent-component analysis (ICA)

Independent-component analysis is a statistical data-driven data analysis method, which is used for discovering hidden factors of a given data set. ICA is usually used for blind source separation or feature extraction. ICA assumes that the data are a combinations of linearly mixed, nongaussian independent components [2]. The method cannot separate gaussian components from each other, and thus the assumption of nongaussianity is made. However, if only one component is normally distributed, the model can be estimated.

In matrix notation, the linear relationship between the observed variables $\boldsymbol{x}$ and component variables $\boldsymbol{s}$ can be written as

$$\boldsymbol{x} = \boldsymbol{A}\boldsymbol{s}, \tag{4.6}$$

where $\boldsymbol{A}$ includes the weights for linear mixing. Both $\boldsymbol{A}$ and $\boldsymbol{s}$ are thus unknown matrices.

Equation 4.6 can be written for N independent components and M data

points as

$$\begin{bmatrix} x_1 \\ x_2 \\ . \\ . \\ . \\ x_M \end{bmatrix} = \begin{bmatrix} a_{11} & a_{12} & . & . & a_{1N} \\ a_{21} & a_{22} & . & . & a_{2N} \\ . & . & . & . & . \\ . & . & a_{ij} & . & . \\ . & . & . & . & . \\ a_{M1} & a_{M2} & . & . & a_{MN} \end{bmatrix} \begin{bmatrix} s_1 \\ s_2 \\ . \\ . \\ . \\ s_N \end{bmatrix}. \tag{4.7}$$

Each column of $\boldsymbol{A}$ represents the weighting of the corresponding independent component s_j.

ICA can be implemented using several different algorithms. We used an iterative method called fast fixed-point algorithm [22].

4.3.1 Preprocessing for ICA

Variables s_j are assumed to be nongaussian with unit variance. Sphering, also called pre-whitening, is a standard process carried out with Principal Component Analysis (PCA) [22]. A new set of variables $\boldsymbol{v}$ is obtained, for which

$$\boldsymbol{v} = \boldsymbol{M}\boldsymbol{x}. \tag{4.8}$$

Components of $\boldsymbol{v}$ are uncorrelated and their variance equals unity. For expectation value E, this means $E\{\boldsymbol{x}\boldsymbol{x}^{\mathbf{T}}\} = \boldsymbol{I}$ [22]. The whitening operation, carried out as a pre-processing method before implementation of the actual ICA algorithm, has an important role in reducing the complexity of the problem, as uncorreletedness can be considered as a weaker form of independence [2].

The dimension of the new mixing matrix $\boldsymbol{M}$ is reduced to N and it is orthogonal as shown below, which diminishes the workload as it can be determined with fewer parameters than some arbitrary matrix $\boldsymbol{A}$.

We rewrite Equation 4.6 in the form

$$\boldsymbol{v} = \boldsymbol{M}\boldsymbol{x} = \boldsymbol{M}\boldsymbol{A}\boldsymbol{s} = \boldsymbol{B}\boldsymbol{s}, \tag{4.9}$$

where $\boldsymbol{B} = \boldsymbol{M}\boldsymbol{A}$ satisfies the definition of orthogonality

$$E\{\boldsymbol{x}\boldsymbol{x}^{\mathbf{T}}\} = E\{\boldsymbol{B}\boldsymbol{s}(\boldsymbol{B}\boldsymbol{s})^{\mathrm{T}}\} = \boldsymbol{B}E\{\boldsymbol{s}\boldsymbol{s}^{\mathbf{T}}\}\boldsymbol{B}^{\mathbf{T}} = \boldsymbol{B}\boldsymbol{B}^{\mathbf{T}} = \boldsymbol{I}. \tag{4.10}$$

A linear combination of the whitened variables can be written as $\boldsymbol{y} = \boldsymbol{w}^{\mathbf{T}}\boldsymbol{v}$, or in a form $\boldsymbol{y} = \boldsymbol{w}^{\mathbf{T}}\boldsymbol{B}\boldsymbol{s} = \boldsymbol{z}^{\mathbf{T}}\boldsymbol{s} = \sum_j z_j s_j$. Thus $\boldsymbol{y}$ is a linear combination of the individual signal sources. We add a restriction $\|\boldsymbol{w}\| = 1$, which is later needed to make sure that there is a local minimum or maximum

for the optimization problem [2]. Orthogonality of matrix $\boldsymbol{B}$ means that also $\|\boldsymbol{z}\| = 1$.

We now need to introduce the central limit theorem, which states that a sum of a large number of independent and identically distributed random variables with finite mean and variance tend towards gaussian distribution [2]. Thus the combination of these kinds of distributions is more gaussian than any of the individual distributions. In practice, we can use a weaker form of the theorem. In applications, such as ICA, the theorem seems to hold even if the variables are not identically distributed and the sum includes only fairly small number of sources (i.e. 10 or more) [2].

Based on the central limit theorem, the linear combination of independent variables, $\boldsymbol{y}$, becomes least gaussian when it equals only one independent component s_j that has the least gaussian distribution of them all. This utilization of the central limit theorem is the reason why independent component analysis searches for nongaussian components. Naturally, a measure for gaussianity of a distribution is needed and one such measure is kurtosis [22]. The search for local extrema of kurtosis of linear combination of whitened variables $\boldsymbol{v}$ can one-by-one extract the nongaussian independent variables $\boldsymbol{s}$ [22].

For a random variable $\boldsymbol{y}$, which has zero mean, kurtosis can be written as

$$kurt(\boldsymbol{y}) = E\{\boldsymbol{y^4}\} - 3(E\{\boldsymbol{y}^2\})^2. \tag{4.11}$$

Applying the calculation rules of kurtosis [2], we obtain

$$kurt(\boldsymbol{y}) = kurt(\boldsymbol{w^T v}) = kurt(\boldsymbol{z^T s}) = \sum_j z_j^4 kurt(s_i). \tag{4.12}$$

Kurtosis is zero for a gaussian variable, and variables with non-zero value for kurtosis are called subgaussian (kurtosis smaller than zero) or supergaussian (kurtosis larger than zero). The extreme value of kurtosis can be found by either maximizing or minimizing it; usually maximization of absolute value is used [2]. Extreme points, as discussed above, are obtained when $\boldsymbol{z} = \pm e_j$ (i.e. canonical base vectors) and weight $\boldsymbol{w} = b_j$, a one column of the whitened mixing matrix $\boldsymbol{B}$.

Kurtosis is not always a robust measure, and thus for fast fixed-point algorithm another measure of nongaussianity, called negentropy is used [2]. Negentropy is related to the concept of differential entropy, which is an extension of entropy to be applied for continuous probability distributions [2]. In signal processing, entropy measures the unpredictability and uncertainty of a random variable. For a given variance, variable with the largest entropy is gaussian.

If we have a random variable $\boldsymbol{y}$ and its probability density is $p_y(\boldsymbol{\eta})$, differential entropy is

$$H(\boldsymbol{y}) = -\int p_y(\boldsymbol{\eta}) \ln p_y(\boldsymbol{\eta})\, d\eta. \tag{4.13}$$

Negentropy J for y is

$$J(\boldsymbol{y}) = H\left(\boldsymbol{y}_{gauss}\right) - H(\boldsymbol{y}), \tag{4.14}$$

where $\boldsymbol{y}_{gauss}$ is a random gaussian variable with the same correlation matrix as $\boldsymbol{y}$. Negentropy is zero for a gaussian variable and positive for any other random variable. Because negentropy itself is often difficult to calculate, approximations are used. Most approximations are based on kurtosis, and even better way is to use a method based on expectations of general nonquadratic functions [2].

The maximization problem can be solved by using a gradient method based on the steepest descend or ascend, or by performing a more sophisticated fixed-point algorithm, which has cubic convergence and thus reduces the number of iterations [22]. Iterations are repeated until one column of mixing matrix and duly one independent component is obtained. Each of the N independent components is found one by one, using orthogonalizing projection after each iteration to remove the direction from the $\boldsymbol{w}$.

4.3.2 Spatial ICA, temporal ICA, and fMRI

ICA is increasingly applied in the analysis of fMRI data to study both spatial and temporal structures of brain imaging signals, searching for either spatially or temporally independent components. Thus a given data matrix x of size $N \times M$ is decomposed into a set of patterns and a set of time courses, so that either the patterns or time courses are independent. Currently, ICA is usually applied to seek for spatially independent components, the sites of haemodynamic responses in the brain.

The advantage of ICA compared with a GLM-based approach is that we do not need to construct any task- or stimulus-related models to predict brain activity [23]. This feature is especially useful with more complex stimuli, and spatial ICA has earlier given promising results in the analysis of fMRI data obtained in naturalistic experimental setups ([24],[25],[26]).

In this study we performed spatial ICA, which provides a three-dimensional spatial distribution of brain voxel values and time courses of activation for each spatially independent component; together these sum up to the measured data. In terms of Equation 4.6, $\boldsymbol{x}$ includes the measured fMRI

data, $\boldsymbol{A}$ is a mixing matrix, which includes the time series of independent components, and $\boldsymbol{s}$ is the spatial component map. We searched for significant activation components in the visual areas.

ICA can also be used to separate temporally independent sources. The theory is analogous to the one presented above, but now the independent components are the temporally independent signals and the mixing matrix contains the spatial locations of these components. In this study we followed up the spatial ICA with temporal ICA. Previous studies have found combination of spatial and temporal ICA useful in fMRI experiments [27].

ICA has also been used to remove artifacts from the data before further analysis. In the recorded fMRI data there are always signals that are not related to actual brain activations, but are physiology-related, motion-related or scanner-related artifacts. Such noise sources can be extracted as separate components. In this study we did not examine closer the possible artifact components.

4.3.3 Group ICA

ICA was first used in brain imaging studies to analyze single-subject data, but its use has been extended to provide information on group level. In this study we used a model for performing an ICA analysis on a group of subjects; this procedure is explained below based on Calhoun et al. [28].

Let's assume N statistically independent sources of brain activation for each of the subjects. The number of measured time points is K and the number of voxels V per each subject.

Before the actual estimation of independent components, we can estimate the number of components extracted from the group data. Typically, principal component analysis (PCA) or minimum description length (MDL) [29] is used. In group ICA, the pre-whitening or reduction steps are performed twice to reduce the computational load and speed up the calculation of components.

The first data reduction is performed separately for each subject. For subject p, the preprocessed data are stored in a $K \times V$ data matrix $\boldsymbol{x}$ and $\boldsymbol{M}_p$ is the M-by-K reducing matrix, which is determined by the PCA decomposition and reduces the number of time points from K to M. The reduced data matrix comes from

$$\boldsymbol{v}_p = \boldsymbol{M}_p \boldsymbol{x}_p. \tag{4.15}$$

where $\boldsymbol{v}_p$ is size $M \times V$. As only a square matrix has an inverse, the inverses used here are considered pseudoinverses.

Next the reduced data of each subject is concatenated into one matrix,

which is of size $TM \times V$, for T subjects. The second reduction step reduces the number of time points from TM to N, which is the number of components estimated earlier. Using a reducing matrix $\boldsymbol{G}$ (derived again from PCA decomposition), we obtain

$$\boldsymbol{v}_{all} = \boldsymbol{G} \begin{bmatrix} \boldsymbol{M}_1\boldsymbol{x}_1 \\ \boldsymbol{M}_2\boldsymbol{x}_2 \\ . \\ . \\ \boldsymbol{M}_M\boldsymbol{x}_M \end{bmatrix}, \tag{4.16}$$

where $\boldsymbol{v}_{all}$ is the matrix sized $N \times V$ used for ICA estimation.

For visualization, we can display the voxels contributing most strongly to a particular component map by scaling the voxel values to z-scores (a dimensionless, statistical quantity derived by subtracting mean of voxel weights from an individual score and then dividing the difference by the standard deviation). It is possible to reconstruct single-subject data from the group ICA results.

We performed the independent component analysis using SPM2-compatible Matlab Group ICA of fMRI Toolbox (GIFT), version v1.3b [30]. We used the data of both sessions of all 8 subjects. Estimation of the number of ICs with the minimum description length (MDL) criteria [29] resulted in 57 ICs to be extracted from the data. The ICs were identified with FastICA algorithm [22] included in the GIFT Toolbox.

To summarize the methodological aims, we wanted to compare GLM and ICA in the analysis of fMRI data collected during naturalistic visual stimulation. Earlier studies have suggested that these two methods, complementary to each other, are suitable for group analysis and that they can detect similar, but not identical activations [31][26]. In the study by Calhoun et al. [31] (10 subjects), the GLM-based analysis, with classical hypothesis-led approach, seemed to be more selective and sensitive than the data-driven ICA. Malinen et al. [26] (6 subjects) reported that GLM-derived activations were often less extensive than the ones derived with ICA. Figure 4.1 sums up the basic ideas and differences between ICA and GLM.

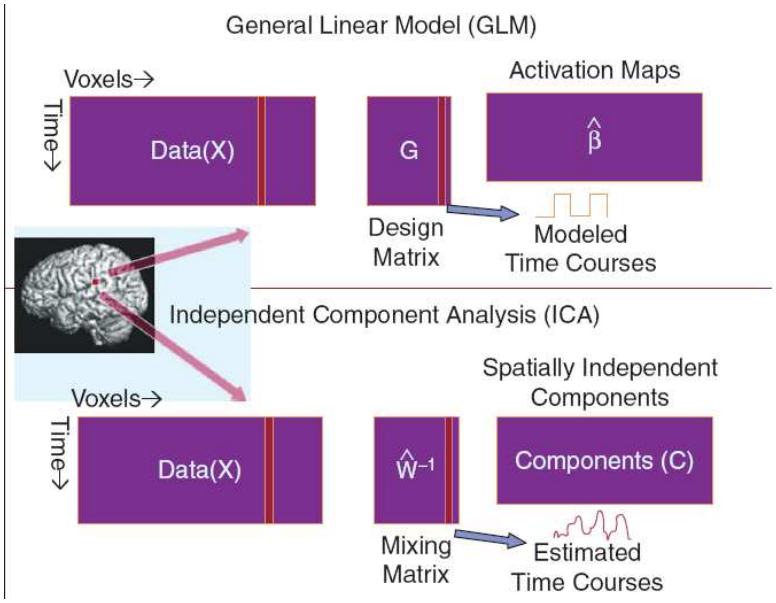

Figure 4.1: A comparison of GLM and ICA. GLM needs a design matrix to model the fMRI time course, whereas spatial ICA requires no model, but estimates the time courses as well as the haemodynamic sources (adapted from [3]).

Chapter 5

Results

5.1 Results of GLM

Figure 5.1 shows the factorial design of the experiment, with two factors and two levels for each factor. The first factor is bird (BIRD), which is still or moving and the other factor is background (BGRD.), which is either gray or natural environment. We carried out a two-way analysis of variance for individual contrast images of the four different conditions acquired with GLM-analysis.

The main effects for the two factors are shown in Figure 5.2 with threshold $p = 0.001$. There were no statistically significant interactions with $p = 0.001$. The main effect of background in Figure 5.2 shows activations in visual areas V1/V2, and the area might cover regions of both central and peripheral visual field. Two other regions, located bilaterally in fusiform gyrus, were also activated. The main effect of bird showed activation in visual motion area V5/MT, precuneus and left middle frontal gyrus, which could correspond to frontal eye field.

We also studied effects of the four different stimulus conditions on the group level. Figure 5.3 presents the t-maps. The condition STILL+GRAY does not show any significant activation clusters. When the movement is added (MOVE+GRAY), the lateral occipital areas of the cortex activate. The condition of still bird on natural background (STILL+NAT) activates the occipital visual cortex. The moving bird with natural background (MOVE+NAT) keeps the activation of occipital areas and also activates more lateral areas.

Table 5.1 presents all the locations of activations for the main effects and different conditions in MNI coordinates. There were also several significant activation clusters outside the occipital areas, i.e., in the frontal gyrus.

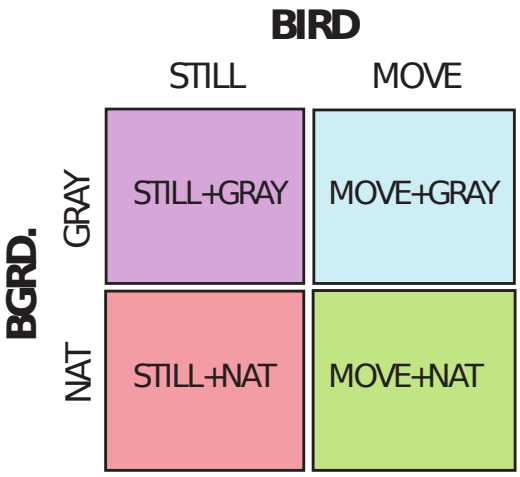

Figure 5.1: Factorial design of the experiment.

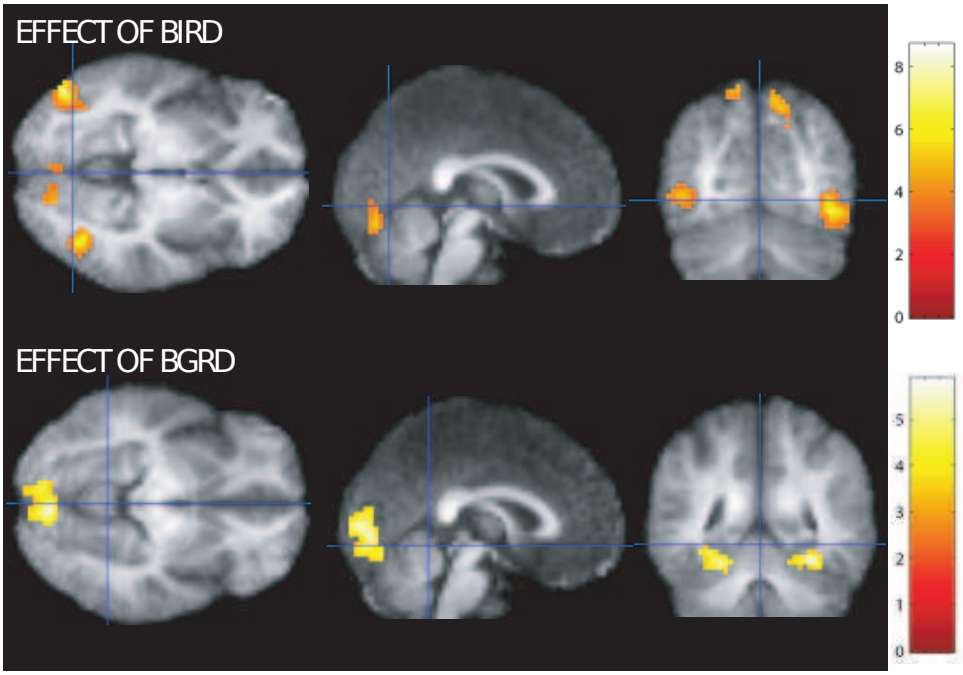

Figure 5.2: Main effects with $p < 0.001$.

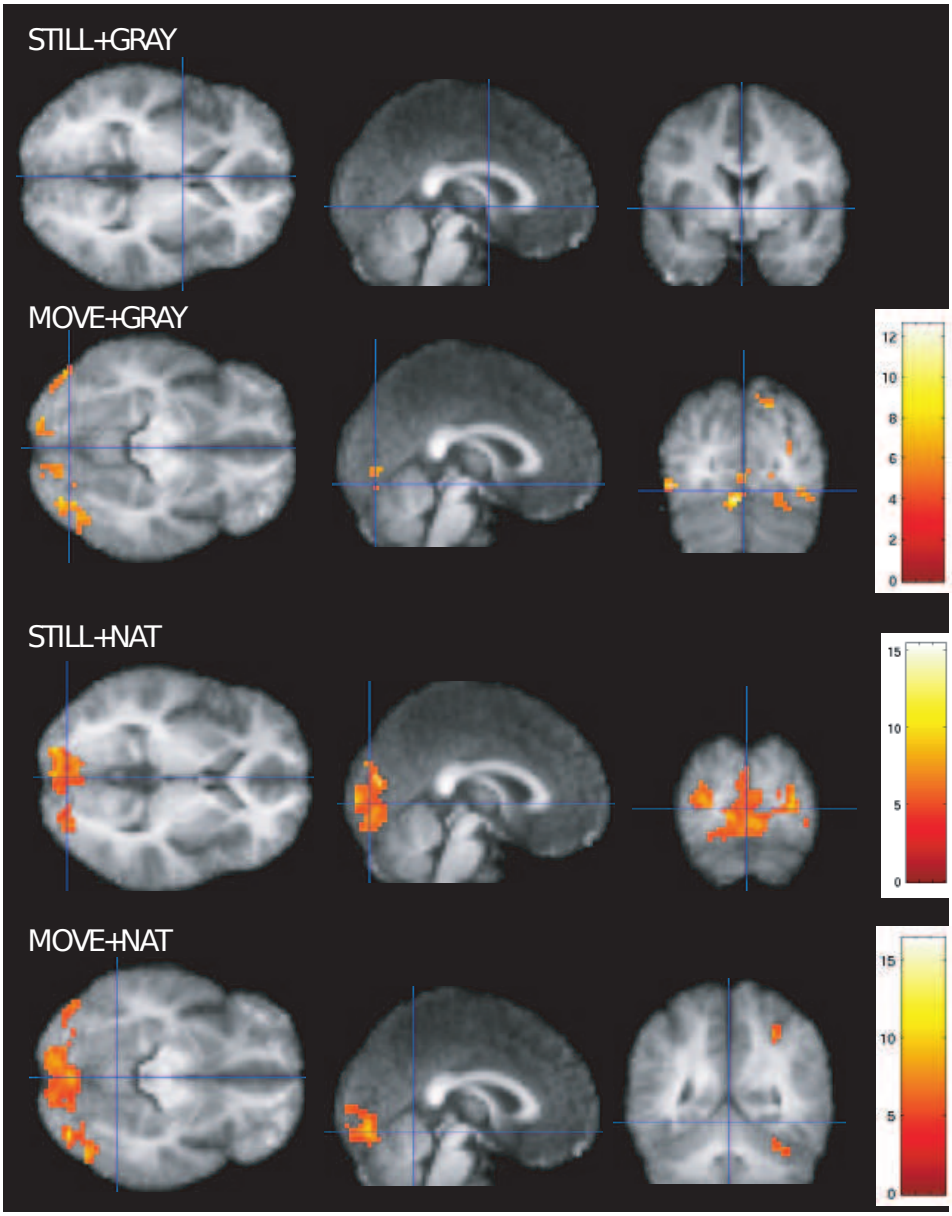

Figure 5.3: Results of GLM-based group analysis with $p < 0.001$.

Table 5.1: MNI coordinates of significant activations obtained with GLM-analysis

Location	**Group t-maps**		
	x	**y**	**z**
Effect of BGRD.			
V1/V2	–6	–87	3
fusiform gyrus	–21	–42	–15
	33	–48	–18
Effect of BIRD			
V5/MT	45	–69	–9
	–48	–78	–6
precuneus	9	–78	51
	–15	–72	63
left sup./mid. front. gyrus	–21	–9	54
left lingual gyrus	–3	–78	–15
Effect of STILL+NAT			
V1/V2	–3	–96	0
fusiform gyrus	30	–57	–27
inf./mid. occ. gyrus	–30	–90	9
	30	–87	3
precuneus	30	–69	51
inf. front. gyrus	57	18	15
Effect of MOVE+GRAY			
V5/MT	48	–75	–15
	–48	–78	–6
mid. occ. gyrus	27	–87	6
	–24	–93	6
precuneus	15	–81	45
Effect of MOVE+NAT			
V1/V2	–9	–93	–12
V5/MT	48	–72	–12
	–48	–78	–6
fusiform gyrus	36	–60	–15
mid. occ. gyrus	–27	–78	18
	30	–75	18
sup./mid. front. gyrus	33	–6	45
right intrapar. sulcus	30	–54	–45
precuneus	15	–81	45
	–15	–81	45

5.2 Results of ICA

Out of the 57 independent components estimated, seven included posterior brain areas. We selected five components, whose locations seemed physiologically feasible in terms of our knowledge of the organization of the visual cortex and a previous ICA study [26], for more detailed analysis. Figure 5.4 shows results of the group analysis, the spatial z-maps of ICs in the occipital and occipito-temporal cortex; selected threshold $z = 3.09$ corresponds to the $p = 0.001$.

Red and blue components, which cover the calcarine cortex, coincide with representations of lower and upper central visual fields, respectively, in the V1/V2 cortex. Anterior to those, the pink component corresponds to the peripheral visual field. The green component is located in the lateral occipital areas, including the posterior convexial cortex. The most lateral, orange component comprising two bilateral activation clusters, represents the visual motion-sensitive area MT/V5. Figure 5.5 shows an magnification of one of the slices.

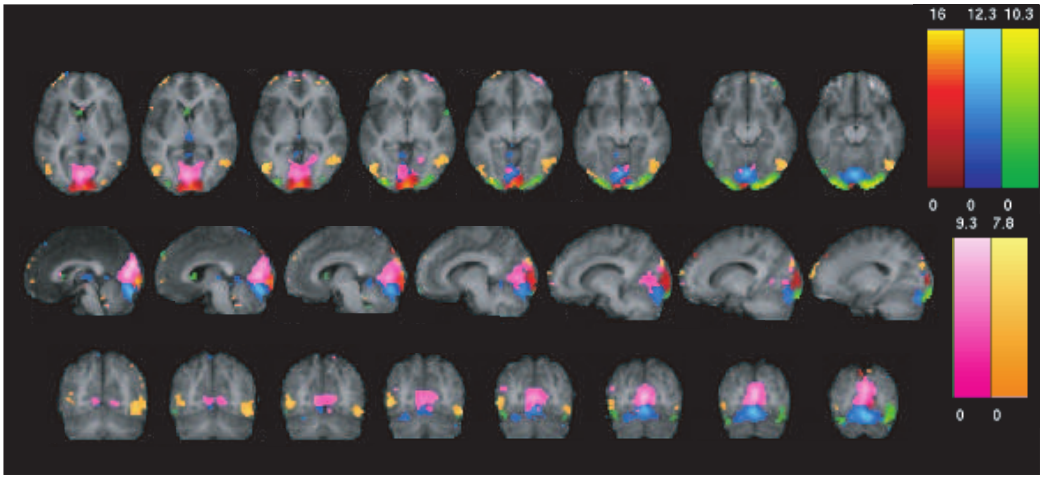

Figure 5.4: Results of ICA analysis in visual cortex, $p < 0.001$.

Table 5.2 presents the MNI coordinates of the activation maxima of these independent components. For some components in Table 5.2, we also calculated submaxima if the maxima did not seem to fully represent the activation cluster of interest. For the component of the peripheral visual field, the coordinates of the actual maximum voxel are $x = 0$, $y = -87$, $z = 24$. This activation might actually represent a retinotopic area at the posterior bank of the parieto-occipital sulcus, which is activated by peripheral visual stimuli [32].

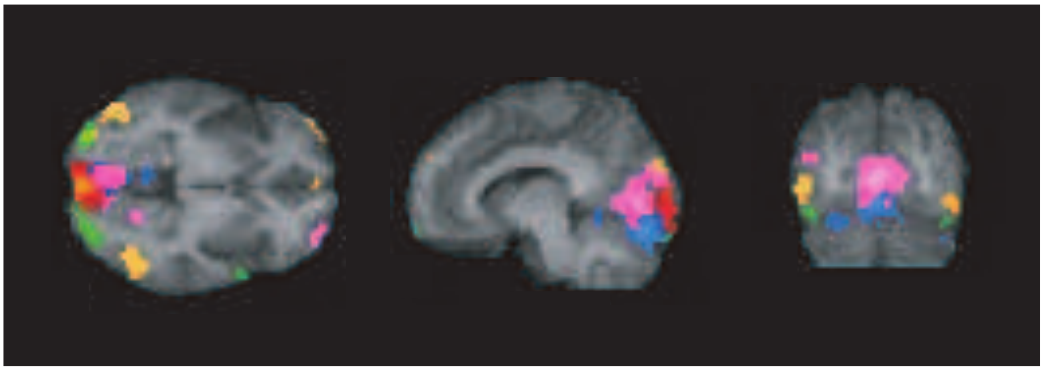

Figure 5.5: Results of ICA analysis in visual cortex, closer look.

Table 5.2: MNI coordinates of independent components

Location	**Group z-maps**		
	x	**y**	**z**
V1/V2, lower central VF	0	–96	–3
V1/V2, upper central VF	–9	–87	–24
Peripheral visual field	0	–78	6 ∗
Inferior occipital lobe	15	–96	–24
	–21	–99	–18
V5/MT	–51	–72	0
	48	–75	0 ∗

Submaximum ∗
Abbreviations: VF,visual field

Figure 5.6 presents the time courses of the selected components, normalized to z-scores. The time course of each component is plotted in the same figure with the color-coded stimulus sequence. Time courses of individual ICs are plotted together in Figure 5.7.

The time courses for the two components of central visual field behave very similarly, which further strengthens the hypothesis that they are the two components corresponding to the same visual field. Components of central vision seem to react strongest to the condition of moving bird with background, during which the signal always rises above the zero level. The behaviour of component of peripheral vision is quite variable and complicated. At the beginning of every block with moving bird, either with or without background, there is a clear peak in the signal. Interestingly, the signal also peaks at the beginning of every rest block. Similar behaviour can be seen in the time series of the component in the posterior convexial cortex, with sharp transient

activation peaks at the beginning of stimulus blocks as well as during them. The time course of V5/MT resembles the time courses of central-vision ICs, though it seems to be a little bit more variable, and it peaks at every block with the moving bird. For the components of central visual field, the individual IC time courses are similar, but for the components of peripheral visual field and convexial cortex there is much more intersubject variation in the time courses. The time courses of the V5/MT component are quite synchronized between subjects.

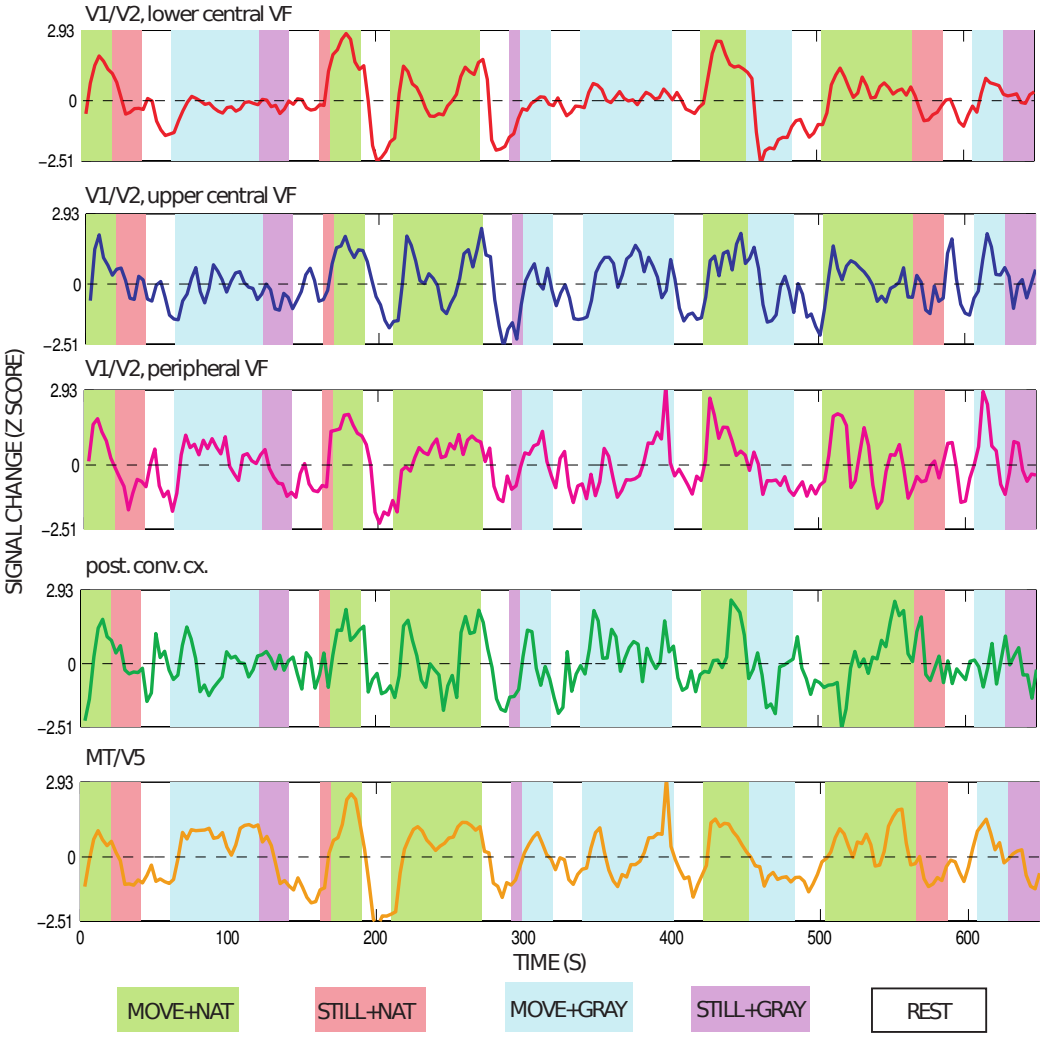

Figure 5.6: The time courses of the selected independent components.

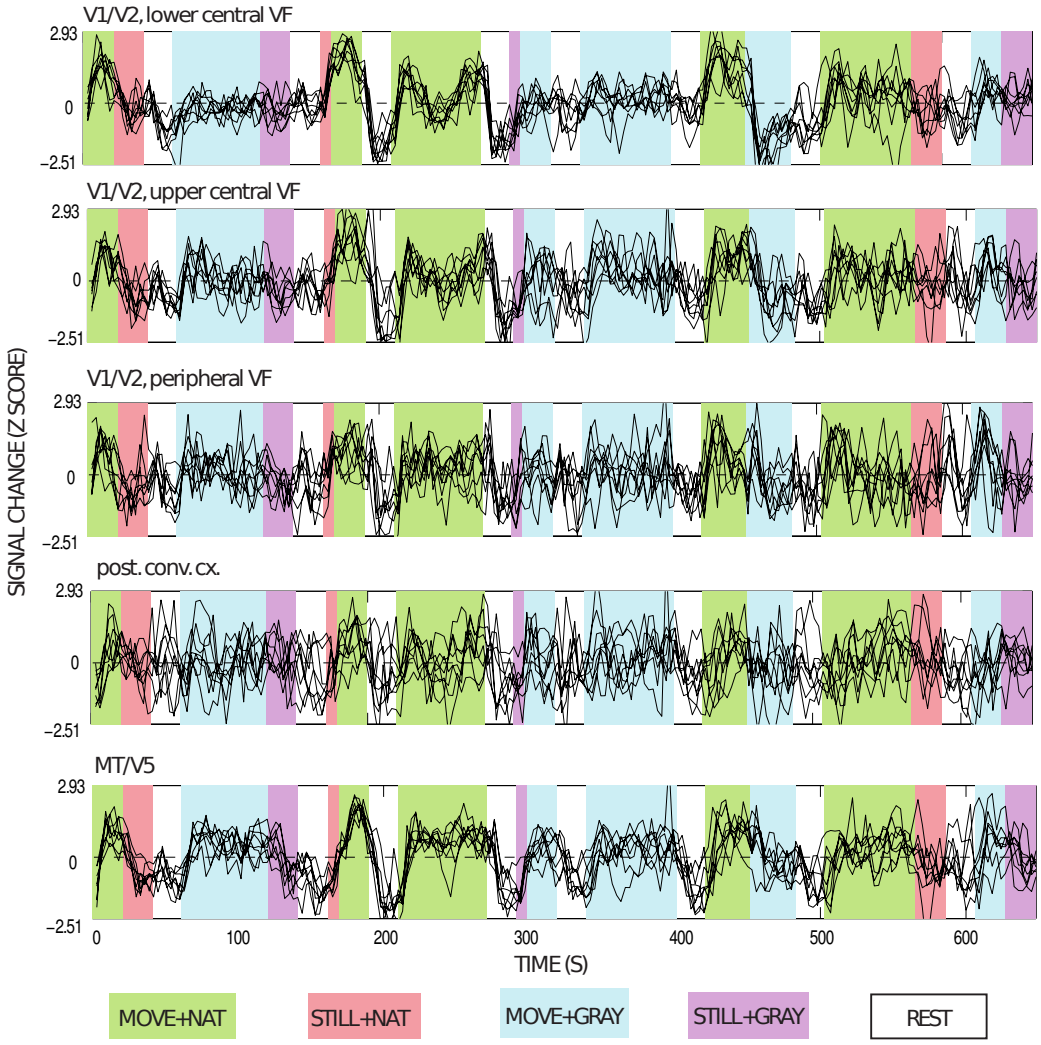

Figure 5.7: All the 8 subjects' time courses of the selected independent components.

From these group results, it is possible to reconstruct the individual subjects' maps and time courses. As the experiment comprised two identical stimulus sessions and thus two separate IC maps were available for each subject and for each component, we next calculated the mean image for each subject for the five components of interest.

Figure 5.8 shows the results of random-effects analysis. Using the same statistical significance ($p = 0.001$) as for the group ICA z-maps and GLM-based analysis, significant activations were obtained only for the component corresponding to the lower central visual field. The location of the activation matched to the IC of the group analysis, although the activation covered only a fraction of the IC. To obtain any significant activations for the four other components, we had to raise the threshold to $p = 0.01$. This result is in line with the level of synchronization between individual time courses, which was low for, implying that the individual brains might not have the same neural activations at the same locations. The behaviour of component V5/MT seemed similar across subjects, but it was not statistically significant in random-effects analysis, either.

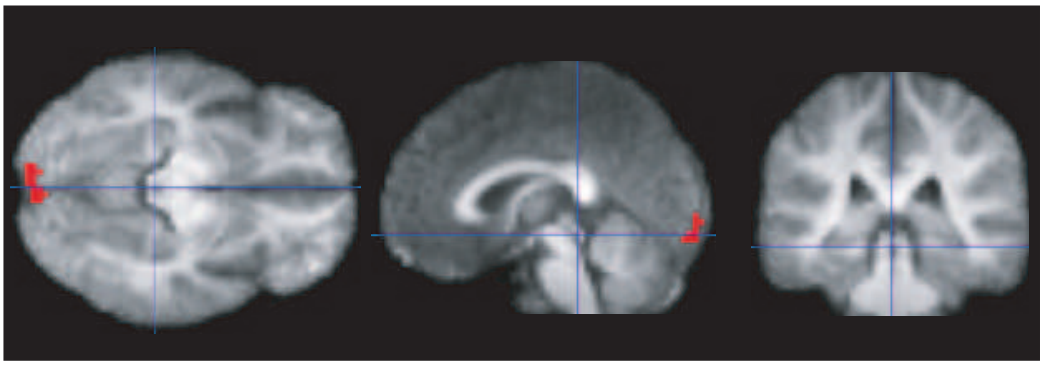

Figure 5.8: Individual ICs t-tested at group level, $p < 0.001$.

Comparison of the results for GLM and ICA, presented in Tables 5.1 and 5.2, shows that the two methods yield similar activations in the occipital areas. GLM associates the activation of the early visual areas with the natural background, and ICA reveals the same area and also divides it into components of lower and upper central visual fields and peripheral visual field. Visual motion area V5/MT was also identified with both methods. The GLM results suggest that the activation of this area is associated with moving stimuli, and the time course of the IC agrees with the result, with an activation peak at the beginning of every block with moving bird.

One interesting component in the parieto-occipital area, similar to some GLM-derived activations, was found bilaterally in the parietal lobe with MNI

coordinates $x = -27$, $y = -75$, $z = 48$ and $x = 24$, $y = -78$, $z = 48$; it likely to covers superior posterior parietal lobe involved in smooth-pursuit eye movements.

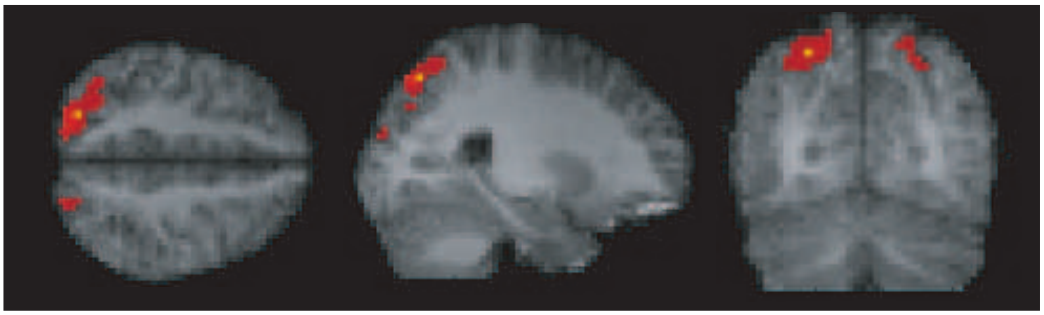

Figure 5.9: Component related to superior posterior parietal cortex activation, revealed by group ICA, $p < 0.001$.

We also wanted to examine components that are not stimulus-related, but could be part of the so-called intrinsic or default-mode networks ([26, 33, 34]). It has been suggested that the fluctuation in the BOLD signal observed during rest could be related to neuronal baseline activity, although some of them could also be caused by other physiological phenomena (such as cardiac pulsation or respiration) [33]. Resting-state patterns have earlier been identified using correlation and IC analysis methods, with and without presence of external stimuli. Even during continuous natural stimulation, the brain maintains its intrinsic activation [34]. Group ICA used in this study enables to search for resting-state networks consistent between all subjects.

Figure 5.10 shows resting-state components. The components were selected using earlier studies ([26, 33]) as reference. Figure 5.10A might represent so-called default-mode network (described by [35]) comprising the prefrontal, posterior cingulate cortex, the inferior parietal gyrus. In our case, though, the activations of these areas seem very weak or even absent, which could be due to the fact that for most part of the stimulus session, the subject were performing a task, which required both attention and concentration.

Interpretation of the time courses of these group level results (see Figure 5.11) is not straightforward. If resting-state networks are representing intrinsic, stimulus-independent mental processes of each individual, there is no reason to expect any synchronized time behaviour between individuals. Closer look at each subject's time courses (Figure 5.12) revealed that they in fact seemed to behave independently of each other, without any clear relation to the external stimulation.

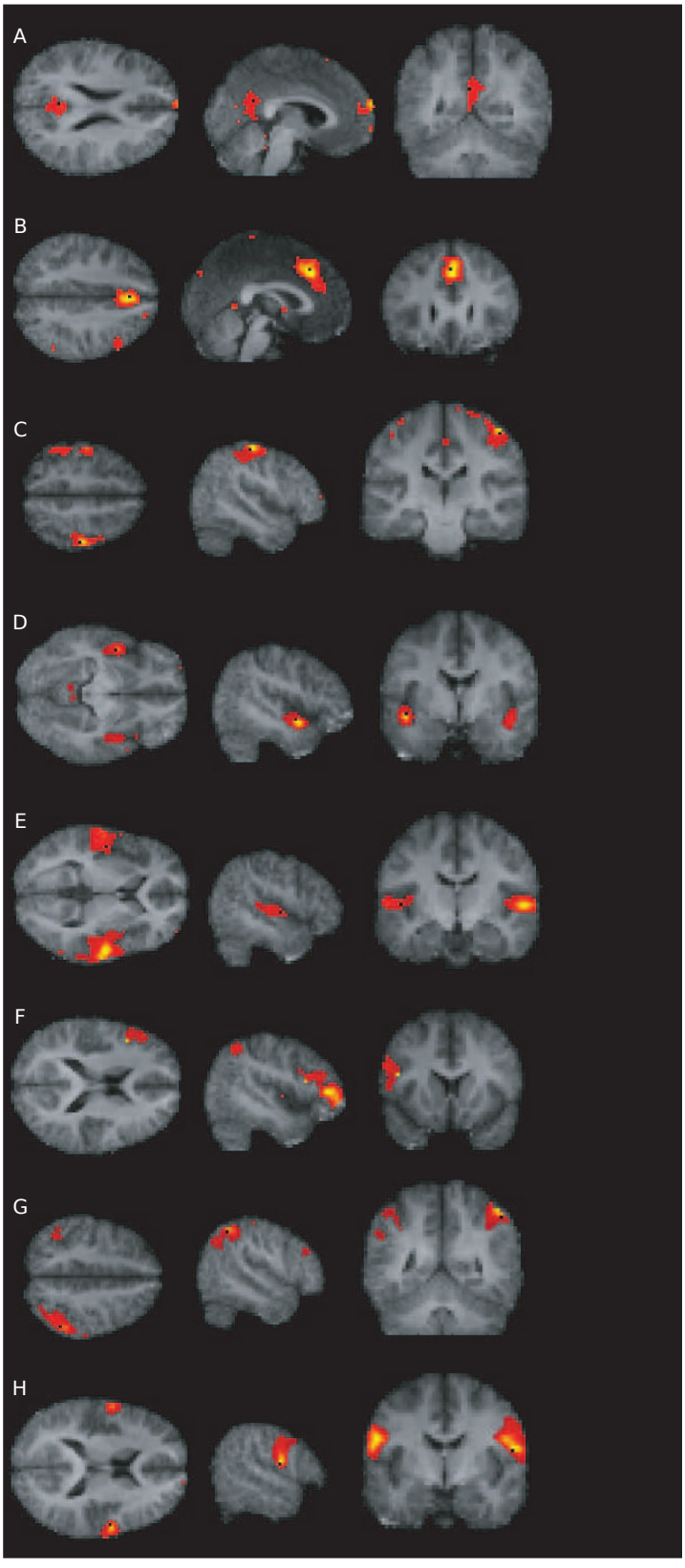

Figure 5.10: Resting state-components revealed by ICA, $p < 0.001$.

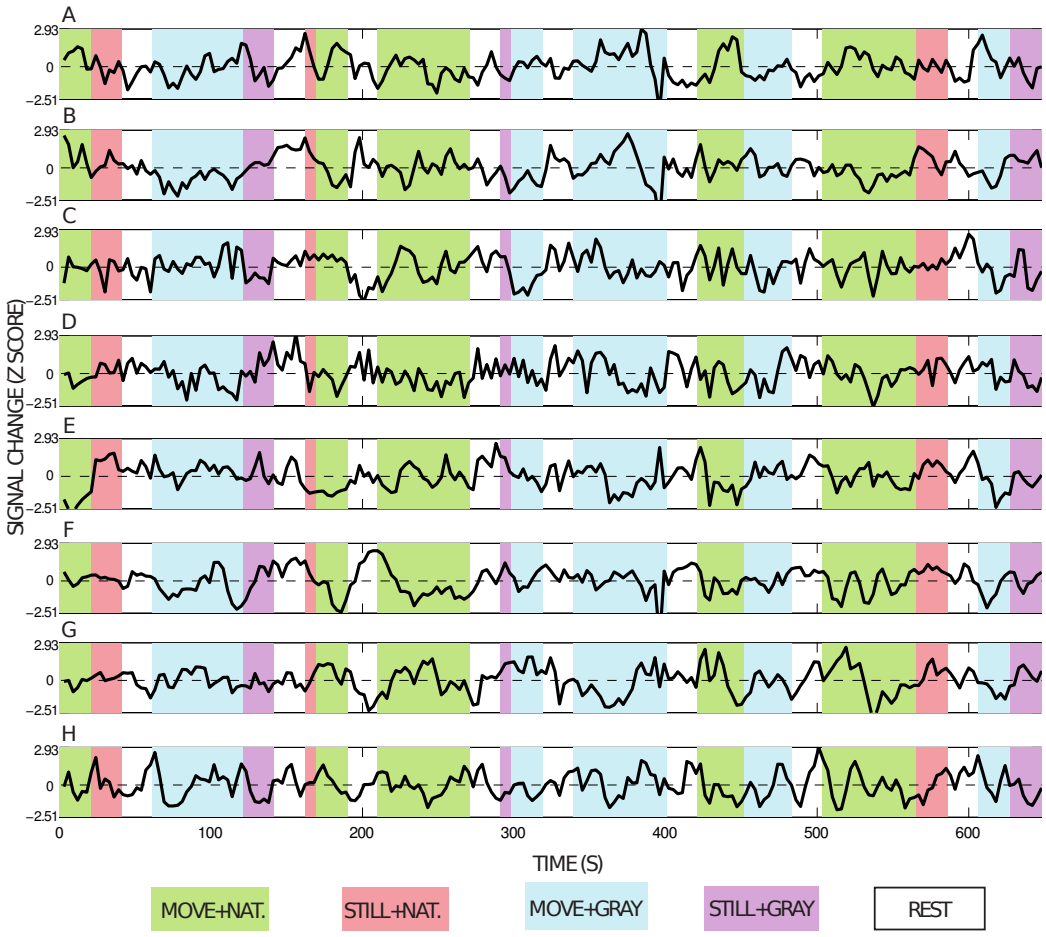

Figure 5.11: The time courses of the selected resting-state independent components.

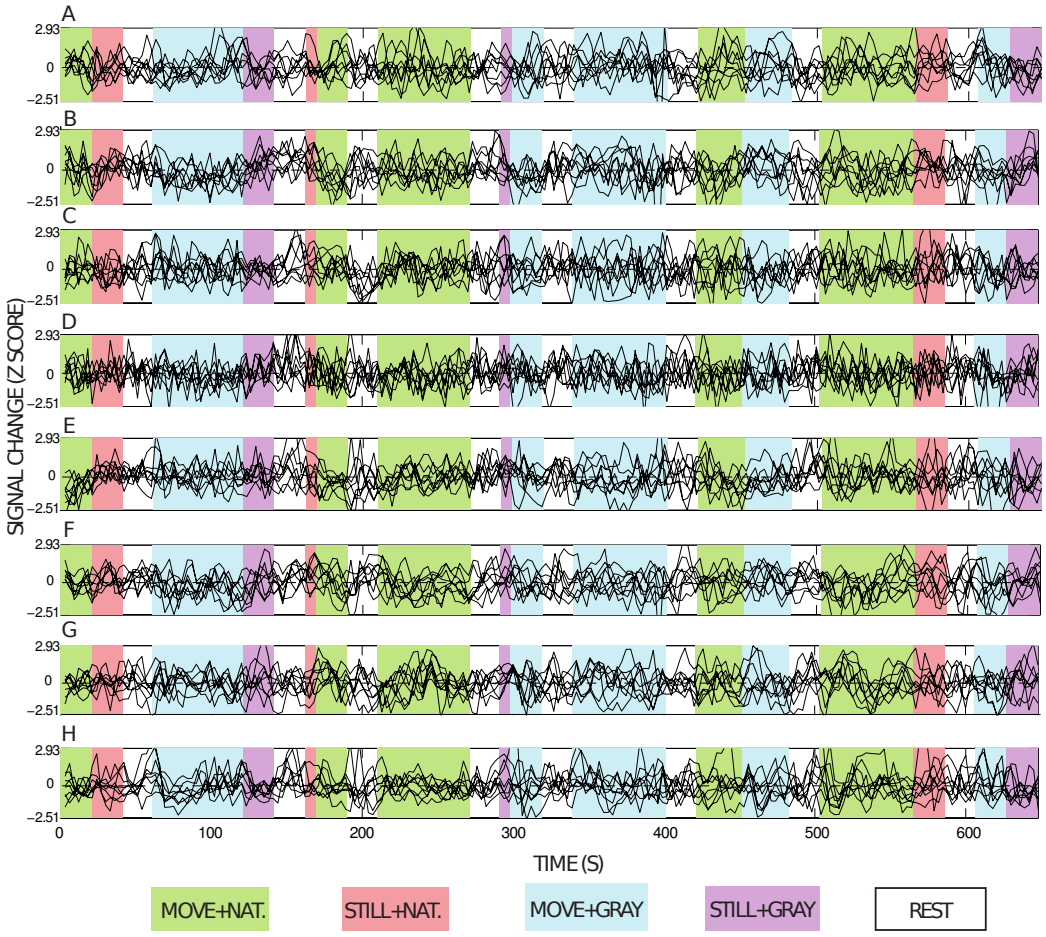

Figure 5.12: All the 8 subjects' time courses of the selected resting-state independent components.

Chapter 6

Discussion

We studied brain processing of visual information during naturalistic viewing conditions. The stimuli in this fMRI study were videos, with a bird still or moving, with or without natural environment on the background. The aim was to compare the results of two analysis methods, independent component analysis and the general linear model. The methods provided distinct and significant information of brain processing during the stimulation, and are discussed separately below.

6.1 GLM

The GLM-based analysis revealed activations both inside and outside the visual cortex. The main effect of background showed significant activations in central and peripheral visual areas and in the fusiform gyrus. Interestingly, although the stimulus on fovea remained the same throughout the experiment, as the subject was fixating on the bird, the background seemed to cause the activation in the areas corresponding to central visual field. One explanation could be that the subjects' center of gaze might have wandered more during natural background condition, but at least the eye-tracking data, studied while 3 subjects were fixating the still bird, did not support this hypothesis. The standard deviation of the fixation did not show any tendency to be bigger for STILL+NAT than STILL+GRAY condition.

The main effect of bird was activation in visual motion area V5/MT, superior posterior parietal cortex (precuneus) and left middle frontal gyrus, which could correspond to frontal eye field. These areas are involved in functional processing of smooth pursuit eye movements [36] as well as in maintaining voluntary visual attention. Pursuit eye movements as associated with activation of frontal eye fields, parietal eye fields in intraparietal cortex,

supplementary eye field in medial superior frontal cortex, area V5/MT and precuneus [36][37]. In smooth-pursuit eye movements, the task is to maintain visual target within the fovea when either the stimulus or individual is moving, in our study, the subject followed a moving or still bird. The different areas related to smooth pursuit eye-movements were also activated for the two conditions with moving bird (see Table 5.1). The effect of bird included activations in lingual gyrus, which is related to visual spatial attention and working memory [38].

Studying the four different stimulus conditions, the difference between the two conditions without background was that when the bird was moving, we could see the activation clusters in the lateral occipital areas, which most likely included, i.e., the visual motion-sensitive area MT/V5. With background, the central areas of visual cortex activated, corresponding most likely to visual areas V1 and V2; including both areas of central and also peripheral vision. Similarly as with the no-background condition, the difference between moving and still bird with background was that the movement presented activation in the lateral occipital areas. All the three conditions also triggered activations outside the visual cortex, which could be related to pursuit eye movements, object-area activations or higher cognitive functions.

The representation of different visual objects in human brain is organized around lateral-occipital complex (LOC) [39]. LOC consists of several subdivisions, two main areas are the dorsal region called lateral occipital (LO) and the more ventral in posterior fusiform gyrus (pFS) [40]. The neighbourhood of these two regions includes a large number of additional regions involved in object recognition.

Various studies have demonstrated that different regions in the occipitotemporal cortex show preferential activation to different object categories, i.e., pFS is termed fusiform face area (FFA) as it shows strongest response to faces, and medial fusiform gyrus (termed collateral sulcus or CoS) responds strongest to images of building or scenes. Preferential areas for other objects also exist.

Since in our study the objects presented in stimuli are mainly houses and landscapes, it is reasonable to assume that the activations in the lower brain surface are mainly located around CoS. Other areas, which also respond preferentially to images of houses and scenes are the transverse occipital sulcus (TOS) and parahippocampal place area (PPA)[41], which did not show any activations for the main effect of background. It should be noted that activation is probably not entirely restricted to the CoS, but also extend to areas which respond maximally to other object categories [42], as stimulus videos included several separate objects (road sign etc).

It has been shown that PFs and CoS maintain their selectivity under free

viewing of natural and complex scenes [43]. In this study, when subjects were following a moving object instead of free exploration of the image, the results implied the same.

It should also be noted, that CoS and TOS have strong activation bias to stimuli located in the peripheral visual field [44]. For example, representations of both small and large buildings overlap peripheral visual field representations, and the periphery effect is preserved both with large single object or multiple smaller objects [41]. It has been suggested that objects that need analysis of fine details have central-biased representation and object which need large-scale integration are peripherally biased [41]. In our study, the natural environment with houses and scenery remained in the peripheral visual field during the whole stimulation, which might have enhanced the activation in CoS and TOS.

For all three conditions that showed significant activation clusters, some activations appeared in the middle occipital gyrus, which is another object area responding preferentially to animals [45]. This might be due to the bird, which was the center of gaze during the whole measurement.

Right intraparietal sulcus, which was activated for the still bird on natural background, is another area responding preferentially to buildings and scenery [42]. Activation in the right inferior frontal gyrus, on the other hand, found during the same condition, can be associated with self-awareness-related functions that are inhibited during difficult tasks . Accordingly, the right inferior frontal activation was absent when the bird was moving and the smooth-pursuit task required attention [46].

6.2 ICA

ICA extracted five components in the visual cortex identified according to MNI coordinates and previous knowledge. The areas seemed to correspond to upper and lower central visual fields, peripheral visual field; moreover, parts of posterior convexial cortex and V5/MT were activated as well.

The two components of central vision had very similar time series, which further supports their close relationship. The strongest response of this component was to condition MOVE+NAT, that is, to the most complex of the four stimulus conditions. The behaviour of individual ICs was highly similar across all the subjects for these two components.

The time series of the peripheral-vision IC was very complex, peaking at the beginning of every block associated with the moving bird. One explanation for this could be that when following a moving bird, the stimulus for peripheral vision is changing and is more complex than when fixating a still

image. This cannot be the whole explanation, though, as surprisingly the signal also peaked at the beginning of every rest period. Recent studies about the transient responses occurring at block transitions suggest that transient responses at different regions show some dependence on transition type and specific task [47]. These BOLD transients could have their origin in neuronal activity connected to functional processes related to a beginning or ending of task blocks. Another possibility is that due to the location of this activation, it is contributed by nonphysiological transients [48].

The IC related to the posterior convexial cortex did not seem to have any clear dependence on stimulus type. The signal reacted to all the different stimulus blocks and there were again some reactions to the rest condition, as well. There were also several distinct activation peaks during blocks. The time course of V5/MT component was quite similar to the components of central vision.

We also noted, while comparing the results of group ICA z-maps to the ones given by t-testing the individual ICs on group level, that the group ICA showed significant and more extensive activation with lower thresholds.

We also looked into so-called resting-state components, which are related to neuronal baseline activity. ICA revealed several components, which did not seem to have stimulus-related time courses and which were consistent with the previous studies. For some reason, ICA could not reveal any object-related areas even with lowered threshold, although such areas were identified in GLM-derived activation maps.

Altogether, these results suggest that ICA can provide valid and physiologically significant results in addressing activations of visual cortex during naturalistic viewing conditions. The signal sources in the visual areas coincide with the previous knowledge of the structure of visual cortex, although the interpretation of time series was quite complicated.

Some previous studies with natural stimuli have suggested that the ICA can be a powerful tool when studying activations of different functional areas [26]. In the future, the emphasis of stimuli in brain-imaging studies will likely shift towards more natural and complex stimulation, and ICA can thus reveal us new functional brain areas without making any previous hypothesis about relationship between stimuli and data.

6.3 Conclusions

In future analyses of fMRI data associated with dynamic naturalistic stimuli or tasks, both blind-source separation methods and GLM-based analyses need to be further developed [49]. In addition to ICA, such methods as

reverse correlations and multi-voxel pattern analysis offer insight into understanding effects of stimuli on brain function as well as predicting the stimuli from the brain-activation patterns. The more traditional GLM-method can be combined with stimulus-classifications or verbal reports, which help determining the timing of the cognitive processes [49]. In the current study, both ICA and GLM revealed activations that the other one missed, and thus the methods complemented each other. In the future, the development and use of eye-tracking systems will also reveal more information about the subject's behaviour and attention during real-world experiences.

Bibliography

[1] A. Webb. *Introduction to Biomedical Imaging*. Wiley-Interscience, 2003.

[2] A. Hyvärinen, J. Karhunen, and E. Oja. *Independent Component Analysis*. John Wiley and Sons, 2001.

[3] V. D. Calhoun and T. Adali. Unmixing fMRI with independent component analysis. *IEEE Eng. Med. Biol. Mag. 2006*, 25: 79–90.

[4] J. Hérault and B. Ans. Circuits neuronaux à synapses modifiables: décodage de messages composites par apprentissage non supervisé. *C.-R de l´ Académie des Sciences 1984*, 299(III-13): 525–528.

[5] P. Jezzard, P. M. Matthews, and S. M. Smith. *Functional MRI: an Introduction to methods*. Oxford University Press, 2001.

[6] M. Hämäläinen, R. Hari, R. J. Ilmoniemi, J. Knuutila, and O. V. Lounasmaa. Magnetoencephalography − theory, instumentation, and applications to noninvasive studies of the working human brain. *Rev. Mod. Phys. 1993*, 65: 414–487.

[7] M. F. Bear, B. W. Connors, and M. A. Paradiso. *Neuroscience, Exploring the Brain*. Lippincott Williams and Wilkins, 2001.

[8] F. Crick. *The Astonishing Hypothesis*. Simon and Schuster New York, 1994.

[9] J. G. Nicholls, A. R. Martin, and B. G. Wallace. *From Neuron to Brain*. Sinauer Associates, 2001.

[10] S. Zeki. *A Vision of the Brain*. Blackwell Scientific Publications, 1993.

[11] M. C. Morrone, M. Tosetti, D. Montanaro, A. Fiorentini, G. Cioni, and D. C. Burr. A cortical area that responds specifically to optic flow, revealed by fMRI. *Nature Neurosci. 2000*, 18: 1322–1328.

[12] M. I. Sereno, A. M. Dale, J. B. Reppas, K. K. Kwong, J. W. Belliveau, T. J. Brady, B. R. Rosen, and R. B. H. Tootell. Borders of multiple visual areas in humans revealed by functional MRI. *Science 1995*, 268: 889–893.

[13] E. M. Haacke, R. W. Brown, M. R. Thompson, and R. Venkatesa. *Magnetic resonance imaging − Physical principles and sequence design*. John Wiley and Sons, 1999.

[14] S. Ogawa, T. M. Lee, A. R. Kay, and D. W. Tank. Brain magnetic resonance imaging with contrast dependent on blood oxygenation. *Proc. Natl. Acad. Sci. U.S.A 1990*, 87: 9868–9872.

[15] Presentation software. http://nbs.neuro-bs.com/presentation 4/2006.

[16] MRIcro software. http://www.sph.sc.edu/comd/rorden/mricro.html.

[17] SPM2, Statistical Parametric Mapping, Wellcome Department of Imaging Neuroscience. http://www.fi.ion.ucl.ac.uk/spm.

[18] *The FIL Methods Group: SPM5 manual*. Wellcome Department of Clinical Neuroscience, 2006.

[19] Medical Research Council's Cognition and Brain Sciences Unit. http://www.mrc-cbu.cam.ac.uk/.

[20] J. Talairach and P. Tournoux. *Co-planar stereotactic atlas of the human brain: 3-dimensional proportional system: an approach to cerebral imaging*. New York: Thieme Medical Publishers, 1988.

[21] J. Ashburner, K. Friston, and W. Penny. *Human Brain Function, second edition*. Wellcome department of imaging neuroscience, 2003.

[22] A. Hyvärinen and E. Oja. A fast fixed-point algorithm for independent component analysis. *Neural Comput. 1997*, 9: 1483–1492.

[23] M. J. McKeown, T-P. Jung S. Makeig, G. Brown, S. S. Kindermann, T-W. Lee, and T. J. Sejnowski. Spatially independent activity patterns in functional MRI data during the stroop color-naming task. *Proc. Natl. Acad. Sci. USA 1998*, 95: 803–810.

[24] A. Bartels and S. Zeki. Brain dynamics during natural viewing condition − a new guide for mapping connectivity in vivo. *Neuroimage 2005*, 24: 339–349.

[25] K. N. Carvalho, G. D. Pearlson, R. S. Astur, and V. D. Calhoun. Simulated driving and brain imaging: combining behaviour, brain activity, and virtual reality. *CNS Spectrums 2006*, 11: 52–62.

[26] S. Malinen, Y. Hlushchuk, and R. Hari. Towards natural stimulation in fMRI − issues of data analysis. *Neuroimage 2007*, 35: 131–139.

[27] V. D. Calhoun, T. Adali, G. D. Pearlson, and J. J. Pekar. Spatial and temporal independent component analysis of functional mri data containing a pair of task-related waveform. *Hum. Brain Mapp. 2001*, 3: 43–53, .

[28] V. D. Calhoun, T. Adali, G. D. Pearlson, and J. J. Pekar. A method for making group inferences from functional MRI data using independent component analysis. *Hum. Brain Mapp. 2001*, 14: 140–151, .

[29] Y. Li, T. Adali, and V. D. Calhoun. Estimating the number of independent components for fMRI data. *Hum. Brain Mapp. 2007*, 28: 1251–1266.

[30] Group ICA of fMRI toolbox. http://icatb.sourceforge.net/.

[31] V. D. Calhoun, T. Adali, V. B. McGinty, J. J Pekar, T. D. Watson, and G. D. Pearlson. fMRI activation in a visual-perception task:network of areas detected using the general linear model and independent components analysis. *Neuroimage 2001*, 14: 1080–1088, .

[32] L. Stenbacka and S. Vanni. fMRI of peripheral visual field representation. *Clin. Neurophysiol. 2007*, 118: 1303–1314.

[33] J. S. Damoiseaux, S. A. Rombouts, F. Barkhof, P. Scheltens, C. J. Stam, S. M. Smith, and C. F. Beckhamm. Consistent resting-state networks across healthy subjects. *Proc. Natl. Acad. Sci. U.S.A 2006*, 103: 13848–13853.

[34] Y. Golland, S. Bentin, H. Gelbard, Y. Benjamini, R. Heller, Y. Nir, U. Hasson, and R. Malach. Extrinsic and intrinsic systems in the posterior cortexx of the human brain revealed during natural sensory stimulation. *Cereb. Cortex 2007*, 14: 766–777.

[35] M. E. Raichle, A. M. MacLeod, A. Z. Snyder, W. J. Powers, D. A. Gusnard, and G. L. Shulman. A default mode of brain function. *Proc. Natl. Acad. Sci. U.S.A 2001*, 98: 676–682.

[36] L. Petit and J. V. Haxby. Functional anatomy of pursuit eye movements in humans as revealed by fMRI. *Journal Neurophysiol. 1999*, 81: 463–471.

[37] J. Tanabe, J. Tregellas, D. Miller, R. G. Ross, and R. Freedman. Brain activation during smooth-pursuit eye movements. *Neuroimage 2002*, 17: 1315–1324.

[38] D. Schmidt, B. J. Krause, P. H. Weiss, G. R. Fink, N. J. Shah, M.-A. Amorim, H.-W. Muller, and A. Berthoz. Visuospatial working memory and changes of the point of view in 3d space. *Neuroimage 2007*, 36: 955–968.

[39] K. Grill-Spector, Z. Kourtzi, and N. Kanwisher. The lateral occipital complex and its role in object recognition. *Vision Research 2001*, 41: 1409–1422.

[40] R. Malach, U. Hasson, and M. Harel. The topography of high-order human object areas. *Trends Cogn. Neurosci. 2002*, 6: 176–183.

[41] I. Levy, U. Hasson, M. Harel, and R. Malach. Functional analysis of the periphery effect in human building related areas. *Hum. Brain Mapp. 2004*, 22: 15–26, .

[42] A. Ishai, L. G. Ungerleider, A. Martin, and J. V. Haxby. The representations of objects in the human occipital and temporal cortex. *Journal Cogn. Neurosci. 2000*, 22: 15–26.

[43] U. Hasson, Y. Nir, I. Levy, G. Fuhrmann, and R. Malach. Intersubject synchronization of cortical activity during natural vision. *Science 2004*, 303: 1634–1640.

[44] I. Levy, U. Hasson, G. Avidan, T. Hendler, and R. Malach. Center-periphery organization of human object areas. *Nature Neurosci. 2001*, 5: 533–539, .

[45] L. L. Chao, J. V. Haxby, and A. Martin. Attribute-based neural substrates in temporal cortex for perceiving and knowing about objects. *Nature Neurosci. 1999*, 2: 913–919.

[46] I. I. Goldberg, M. Harel, and R. Malach. When brain loses its self: Prefrontal inactivation during sensorimotor processing. *Neuron 2006*, 50: 329–339.

[47] M. D. Fox, A. Z. Snyder, D. M. Barch, D. A. Gusnard, and M. E. Raichle. Transient BOLD responses at block transitions. *Neuroimage 2005*, 28: 956–966.

[48] V. Renvall and R. Hari. Transients may occur in functional magnetic resonance imaging without physiological basis. *Proc. Natl. Acad. Sci. U.S.A 2009*, 106: 20510–20514.

[49] H. J. Spiers and E. A. Maguire. Decoding human brain activity during real-world experinces. *Trends Cogn. Neurosci. 2007*, 11: 356–365.